The Cryosphere Discuss., https://doi.org/10.5194/tc-2018-237
Manuscript under review for journal The Cryosphere
Discussion started: 22 November 2018

Satellite ice extent, sea surface temperature, and atmospheric methane trends in the Barents and Kara Seas

Ira Leifer[1], F. Robert Chen[2], Thomas McClimans[3], Frank Muller Karger[2], Leonid Yurganov[4]

[1] Bubbleology Research International, Inc., Solvang, CA, USA

[2] University of Southern Florida, USA

[3] SINTEF Ocean, Trondheim, Norway

[4] University of Maryland, Baltimore, USA

Correspondence to: Ira Leifer (ira.leifer@bubbleology.com)

Abstract. Over a decade (2003-2015) of satellite data of sea-ice extent, sea surface temperature (*SST*), and methane (CH_4) concentrations in lower troposphere over 10 focus areas within the Barents and Kara Seas (BKS) were analyzed for anomalies and trends relative to the Barents Sea. Large positive CH_4 anomalies were discovered around Franz Josef Land (FJL) and offshore west Novaya Zemlya in early fall. Far smaller CH_4 enhancement was found around Svalbard, downstream and north of known seabed seepage. *SST* increased in all focus areas at rates from 0.0018 to 0.15 °C yr^{-1}, CH4 growth spanned 3.06 to 3.49 ppb yr^{-1}.

The strongest *SST* increase was observed each year in the southeast Barents Sea in June due to strengthening of the warm Murman Current (MC), and in the south Kara Sea in September. The southeast Barents Sea, the south Kara Sea and coastal areas around FJL exhibited the strongest CH_4 growth over the observation period. Likely sources are CH_4 seepage from subsea permafrost and hydrate thawing and the petroleum reservoirs underlying the central and east Barents Sea and the Kara Sea. The spatial pattern was poorly related to seabed depth. However, the increase in CH_4 emissions over time may be explained by a process of shoaling of strengthening warm ocean currents that would also advect the CH_4 to areas where seasonal deepening of the surface ocean mixed layer depth leads to ventilation of these water masses. Continued strengthening of the MC will further increase heat transfer to the BKS, with the Barents Sea ice-free in ~15 years. We thus expect marine CH_4 flux to the atmosphere from this region to continue increasing.

Keywords: Arctic, methane, sea surface temperature, ice, Barents and Kara Seas, warming, currents, emissions

Highlights:

- Warm, eastwards-flowing Murman Coastal Current penetrates further into the Barents and Kara Seas
- Currents transport heat, driving increasing methane emissions
- Ocean current shoaling enhances shallow methane transport and allows deep methane transport to the atmosphere.
- Franz Josef Land and the west coast of Novaya Zemlya are important, unaccounted and growing CH_4 sources
- Thermogenic methane from hydrates and submerged permafrost likely play an important role.

1. Introduction

1.1 Changes in the Arctic Environment in the Anthropocene

The Arctic has experienced the fastest warming on Earth over recent decades, termed Arctic amplification (Manabe and Stouffer, 1980) with the Arctic Ocean warming at nearly double the rate of the rest of the world's oceans (Hoegh-Guldberg and Bruno, 2010). Arctic amplification is strongly evident in the Arctic sea-ice reductions associated with increasing sea surface temperature (*SST*) (Comiso, 2012; Comiso et al., 2008; Graversen et al., 2008; Hoegh-Guldberg and Bruno, 2010; Overland and Wang, 2013; Screen and Simmonds, 2010; Stroeve et al., 2014).

Multiple positive feedbacks underlie Arctic amplification; such as decreased sea-ice cover increasing solar insolation absorption, thereby decreasing sea ice further, which also increases humidity and thus downwelling infrared radiation (Screen and Simmonds, 2010). These feedbacks can be complex. Poleward humidity transport has been identified as leading to greater downwelling longwave radiation and resultant ice loss in the Pacific Arctic, which increased humidity and downwelling longwave radiation (Lee et al., 2017). The progression of warmer water into the Barents Sea drives local winds that decrease wind-advection of sea ice, with decreased sea-ice *increasing* heat loss by cooling from the atmosphere (Lien et al., 2017). The progressive decrease in Arctic-ice extent underlies numerous oceanic physical (NRC, 2014) and ecosystem feedbacks (Alexander et al., 2018). Retreating ice affects heat transfer, light availability in the water column, momentum transfer (convective and wind mixing), and ocean heat and moisture exchange with the atmosphere. Thus, beyond albedo, sea-ice changes affect weather (NRC, 2014). Data since 1948 show that Arctic Ocean and atmospheric temperatures and storm frequency increased as sea-ice extent and volume decreased (NRC, 2014).

Arctic amplification has implications for seabed methane (CH_4) emissions – particularly that which currently is "sequestered" beneath subsea permafrost – terrestrial permafrost inundated by rising sea level after the Holocene. For example, extensive seabed CH_4 seepage is linked closely with destabilization of subsea permafrost in the East Siberian Sea (Shakhova et al., 2013) with emissions estimated as comparable to those from Arctic Tundra (Shakhova et al., 2015). Warmer seabed temperatures degrade subsea permafrost integrity (Shakhova et al., 2017), enhancing emissions (Shakhova et al., 2015); however, timescales remain uncertain. Subsea permafrost is likely extensive in the Kara Sea, and possibly southeast Barents Sea (Osterkamp, 2010). Another feedback occurs from sea ice reduction, which increases CH_4 flux to the atmosphere by no longer impeding gas transfer.

FIGURE 1 HERE – *Arctic methane map*

The marine Arctic is affected by changes in the terrestrial Arctic, both climate and fresh water and organic material inputs from rivers. Arctic soils contain 50% of the global subterranean carbon pool of which 88% is estimated sequestered in permafrost (Tarnocai et al., 2009). A quarter of this 1670 Pg (1 Pg=10^{15}g) carbon pool may be mobilized into the Arctic Ocean and sub-marginal seas over the next century due to Arctic warming (Gruber et al., 2004). The Arctic and sub-Arctic show strong terrestrial, high latitude, positive CH_4 anomalies for eastern Canada, Alaska, and Western Russia (**Fig. 1**). Still, the Barents Sea, where the most rapid winter ice loss has occurred and which likely will be the first year-round ice-free arctic sea (Onarheim and Årthun, 2017) and the Kara Sea, show the strongest CH_4 anomalies by far.

1.2. Study Motivation

We hypothesize that increases in water column temperature drive subsea permafrost and hydrate destabilization that result in seabed CH_4 emissions, which manifests as increases in lower tropospheric CH_4 over the Barents and Kara Seas. The relationship between seabed CH_4 and atmospheric CH_4 is indirect – seabed CH_4 must be transported through the water column on timescales faster than microbial oxidation timescales. CH_4 transport is by bubbles, diffusion, vertical mixing. We propose that current heat transport is driving increasing seabed emissions. Currents are the major contributor of oceanic heat to the Barents Sea on annual (Lien et al., 2013) and seasonal time-scales (Lien et al., 2017) and towards sea ice loss (Årthun et al., 2012).

Our study investigates this hypothesis using *SST* and lower atmospheric CH_4 for which satellite data 2003-2015 were analyzed for statistically significant trends in the Barents and Kara Seas relative to the Basin trends. Seabed temperatures cannot be observed by satellite, thus we test our hypothesis using *SST* as a proxy, albeit one affected both by currents and other processes including meteorology and solar insolation/long-wave downwelling radiation (i.e., cloudiness and GHGs including CH_4). Still, *SST* variations from these atmospheric and radiative processes only weakly affect the seabed due to stratification.

Satellite data are key as they allow repeat observations of multiple variables on synoptic spatial scales, thus we analyze satellite-derived-*SST*, CH_4, and sea ice extent in cloud free pixels. Trends are analyzed with respect to data on currents and winds to understand how the spatial and temporal distribution of tropospheric CH_4 above the Barents and Kara Seas relates to heat transport into these seas. Specific focus is on areas that become ice-free seasonally and inter-annually. The analysis focuses on localized anomalies and trends (tens to hundreds of kilometers), relative to the overall Barents Sea and thus de-emphasizes processes such as poleward atmospheric moisture transport that affect *SST* on regional scales.

FIGURE 2 HERE – *Map of area and ice extent in January and September*

The approach's potential was revealed in a scoping study of a small area (**Supp. Table S1, Box A2**) in the marginal ice zone where Barents Sea water flows into the St. Anna Trough between Franz Josef Land and Novaya Zemlya (**Fig. 2b, star**). For these pixels, satellite *SST* and CH_4 (0-4 km) were correlated (CH_4 increased with increasing *SST*) for one of two pixel populations (**Fig. 3, Blue oval**). Given that the oceanography, including ice, varies dramatically across the Barents and Kara Seas we test our hypothesis on ten focus areas to elucidate how trends differ across the Barents Sea. Focus areas were large enough to decrease noise by pixel aggregation while small enough to avoid reducing trends by spatial averaging.

FIGURE 3 HERE – *SST vs CH4 for scoping area*

The Cryosphere Discuss., https://doi.org/10.5194/tc-2018-237
Manuscript under review for journal The Cryosphere
Discussion started: 22 November 2018

The Cryosphere Discussions
Open Access

1.3 Sea Surface Temperature (*SST*)

SST is the ocean skin layer temperature and depends on the balance between downwelling and upwelling radiation (modified by clouds and aerosols), and heat transfer between the underlying ocean and overlying atmosphere and evaporative cooling (Frankignoul, 1985). The upper layer of the ocean is well mixed (the WML) by turbulence and windwaves. Thus, persistent (multiple days) *SST* anomalies generally reflect (to some degree) temperature anomalies of the WML but not water below the WML, which is insulated by stratification. Screen and Simmonds (2010) found that the strongest Arctic warming was in the near-surface atmospheric layer and was most strongly related to the retreat of sea ice. Scales are important – atmospheric heat transport in the marine atmosphere tends to be on large spatial scales, whereas currents affect *SST* on smaller scales both near the seabed and near the sea surface.

Solar insolation changes immediately affect *SST*, primarily from cloud cover changes. This effect is removed on daily timescales by cloud filtering. On longer timescales, changes in persistent cloudiness can cumulatively alter upper ocean temperatures (and *SST*). Increased cloudiness decreases incoming short wavelength radiation (cooling) while increasing long-wave radiation (warming) (Lee et al., 2017). However, these two effects largely counter each other with the balance further compensated by humidity and temperature profile changes (Schweiger et al., 2008). Given the canceling effects of persistent cloudiness and that significant changes in cloudiness are not observed outside areas of sea ice retreats, Screen and Simmonds (2010) conclude that "...changes in cloud cover have not contributed to recent [Arctic] warming."

Currents also create persistent *SST* anomalies as do winds. During summer, the warm Barents Sea and Kara Sea currents that flow eastwards and northwards are met by northerly winds that transport cooler air from higher latitudes (Kolstad, 2008). This remains the case in fall for all of the Barents Sea except coastal Norway and Murman where winds track the currents and thus amplify warming (**Supp. Fig. S3**). The transition to north winds occurs offshore around the area of the Central Bank in the eastern Barents Sea. Fall winds further north are from the north and oppose current heating.

1.4 Global and Arctic Atmospheric Methane

Since pre-industrial times, emissions of the potent greenhouse gas, CH_4, have risen by a factor of 2.5 (Dlugokencky et al., 2011), with increases resuming after near stabilization in the late 1990s (Nisbet et al., 2014). On a 20-year timescale, CH_4 has greater radiative impact than carbon dioxide (IPCC, 2007; Fig. 2.21). Several processes may explain this trend including increasing emissions from the Arctic, wetlands, and fossil fuel, and/or decreasing losses from hydroxyl radical (OH) (Ghosh et al., 2015; John et al., 2012; Nisbet et al., 2014; Turner et al., 2016), which are proposed to compensate for decreasing biomass burning (Desjardins et al., 2018). OH concentration decreases with increasing latitude (Liang et al., 2017), enhancing Arctic winter CH_4 lifetime relative to lower latitudes. Arctic OH varies seasonally, imposing an ~10 ppb seasonality in CH_4 concentrations (Thonat et al., 2017).

Current CH_4 inventories have high uncertainty, with projections being even more uncertain (IPCC, 2013; Prather et al., 2012; Saunois et al., 2016). Arctic emissions contribute strongly to future CH_4 budget uncertainty due to Arctic amplification (Graversen et al., 2008) and uncertainty in the timescales of the release of the vast Arctic CH_4 deposits trapped as gas, CH_4 hydrates, and organic material under permafrost and sediments both onshore (Tarnocai et al., 2009) and offshore (Archer et al., 2009). For example, rapid warming of the shallow East Siberian Arctic marginal Sea has degraded submerged permafrost integrity, releasing sequestered CH_4 (Shakhova et al., 2017). Global CH_4 concentrations increase poleward and are highest in the Arctic (Xiong et al., 2016), driven in part by strong CH_4 sources, including seabed emissions, terrestrial riverine runoff (Shakhova et al., 2013), and Arctic terrestrial sources (industrial, permafrost, wetlands, fires, etc.).

Arctic seabed CH_4 sources include thermogenic (geological) seepage (Shakhova et al., 2013), biogenic CH_4 production (James et al., 2016; Reeburgh, 2007) and submerged permafrost, originally from biogenic and/or thermogenic sources (Shakhova et al., 2013). Seabed emissions largely are bubbles or dissolved gas; however, microbial oxidation in near seabed sediments (the microbial filter) limits the importance of dissolved seabed CH_4 fluxes (Reeburgh, 2007). Bubble seepage transports CH_4 directly through the water column and potentially to the sea surface after losses through dissolution. Bubble seepage also indirectly transports fluid with dissolved CH_4 (Leifer and Patro, 2002). The fate of dissolved seep CH_4 depends strongly on its dissolution depth (Leifer and Patro, 2002) with microbial oxidation expected to remove dissolved CH_4 below the Winter Wave Mixed Layer (WWML) (Rehder et al., 1999), whereas dissolved CH_4 in the WWML mostly escapes to the atmosphere. Microbial oxidation timescales are weeks in plumes to decades at ambient deepsea concentrations (Reeburgh, 2007). The fraction of seep CH_4 that dissolves below versus within the WWML depends strongly on seabed depth, volume flux (Leifer and Patro, 2002), plume synergies that include the upwelling flow (Leifer et al., 2009) and bubble surface properties including the presence of surface impurities (Leifer and Patro, 2002). Frequent Arctic storms deepen the WWML significantly and efficiently sparge dissolved CH_4 to the atmosphere (Shakhova et al., 2013). Field studies and numerical modeling show that bubbles can transport some of the seabed CH_4 to the upper water-column and potentially sea surface even for deep sea seepage (to ~1 km) due to plume and deep sea bubble processes (MacDonald, 2011; Rehder et al., 2009; Solomon et al., 2009; Warzinski et al., 2014).

1.5. Airborne and Satellite Observations of Arctic Tropospheric Methane

Although the Arctic covers a vast territory, our knowledge of Arctic processes is highly limited both in spatial and seasonal coverage. This is due to high cost, logistical challenges, and the harshness of Arctic weather. Satellite Arctic observations (since 1979) have advantages for Arctic observations including quick revisit times and global coverage (Leifer et al., 2012) and can fill the significant existing temporal and spatial gaps between the few airborne and field datasets.

Several airborne campaigns have measured Arctic atmospheric CH_4 since 2005: HIAPER Pole-to-Pole Observations (HIPPO), which was ocean-focused (Kort et al., 2012; Wofsy, 2011), Carbon in Arctic Reservoirs Vulnerability Experiment (CARVE), which was Alaska focused (Chang et al., 2014) and the Atmospheric Radiation Measurements V (ARM-ACME) on the Alaskan North Slope during summer and off Spitsbergen by the Facility for

The Cryosphere Discuss., https://doi.org/10.5194/tc-2018-237
Manuscript under review for journal The Cryosphere
Discussion started: 22 November 2018

Airborne Atmospheric Measurements (FAAM) for summer marine data (Myhre et al., 2016). Given the highly extensive spatial scales of the Arctic, these campaigns provide only a few summer snapshots of a highly variable domain. A review is presented in Supplemental Materials.

Satellite observations provide long-term temporal context for airborne campaign data, which are limited in time and often spatially, and often to the summer season when weather is acceptable. Remote sensing measures column gas abundance and thus is independent of potential mismatches between the platform altitude and the altitude of enhanced CH_4. Airplanes may not fly sufficiently low to collect data in the Arctic marine planetary boundary layer (PBL), which often is shallow (Aliabadi et al., 2016).

Satellite CH_4 remote sensing uses spectral features at 1.67 and 2.32 μm in the Short Wave InfraRed (SWIR) (Clark et al., 2009) and around 7.82 μm in the thermal infrared (TIR) (Tratt et al., 2014). CH_4 retrievals for SWIR sensors, which use passive reflective solar radiance, are challenged in the Arctic by high cloud cover, low solar zenith angle, and low reflectivity for ice, snow, and water (Leifer et al. 2013). TIR sensors have significant advantages over SWIR sensors for Arctic marine CH_4 (Leifer et al. 2013). TIR sensors measure upwelling surface emitted radiation, which thus has comparatively shorter path lengths at high latitudes relative to SWIR sensors that measure reflected sunlight. TIR sensors can retrieve CH_4 above low clouds, both day and night, whereas SWIR can only observe during daytime and is extremely difficult in the presence of clouds. Additionally, SWIR sensors are insensitive to altitude. Thus, given that most of the CH_4 column abundance lies close to the surface, SWIR sensors respond strongest to the near-surface atmosphere, whereas TIR retrievals have higher sensitivity to mid-tropospheric CH_4 than to near-surface CH_4 (Xiong et al., 2013). Details on the (InfraRed Atmospheric Sounder Interferometer) (IASI) and Atmospheric InfraRed Sounder (AIRS) TIR instruments and validation are provided in **Supplemental Section S2**.

Based on IASI, Yurganov et al. (2016) found low atmospheric CH_4 anomalies in summer for 2010-2015 with annual Arctic Ocean CH_4 fluxes estimated at ~2/3 terrestrial Arctic fluxes (to the north from 60° N). Positive CH_4 anomalies were observed along the coasts of Norway and the Novaya Zemlya and Svalbard archipelagos primarily November-January (Yurganov and Leifer, 2016a). A breakdown of the Arctic oceanic summer thermal stratification by wind-induced mixing in autumn may underlie this seasonal trend. Such an approach has been proposed for the North Sea due to a breakdown of stratification in the summer and fall (Leifer et al., 2015). Additionally, Yurganov and Leifer (2016b) report significant CH_4 increases during the 2015/2016 winter over the Sea of Okhotsk.

2. Method and Study Design

2.1. Overview

In this study, we characterize several processes by satellite observations aggregated on a monthly basis. Satellite data allow repeat regional observations spanning many years. Specifically, we investigated the relationship between ice-free months, sea surface temperature (*SST*), and the lower tropospheric CH_4 column. We concentrate on five focus areas affected by: (1) Arctic water; (2) combined Arctic and Norwegian Atlantic Current; (3) Barents Sea Polar Front; (4) Murman Current; and (5) the Murman Coastal Current and Novaya Zemlya Current.

Specifically, satellite products for the Barents and Kara Seas are quality reviewed and then analyzed to identify statistically significant trends on both a pixel basis and in focus areas relative to regional trends (**Section 2.2**). The analysis uses relative trends to reduce potential retrieval biases and uncertainty. The use of focus areas allows pixel aggregation to reduce the impact of a highly spatially heterogeneous signal and to reduce the effect of inter-annual spatial shifts, which could appear as local temporal variations.

The analysis investigates these trends in relationship to oceanography and meteorology and data for the Barents and Kara Seas relevant to heat transport to, within, and between the Barents and Kara Seas (**Section 2.3**). This analysis investigates the importance of different processes to improve our understanding of the fate of seabed CH_4 emissions.

2.2. Methodology

2.2.1 Satellite data

AIRS CH_4 data (version 6) are publicly available from NASA Goddard Space Flight Center (GSFC) since 2002 (AIRS Science Team/Joao Texeira, 2016). CH_4 data for 2003–2015 are retrieved by the NOAA Unique Combined Atmospheric Processing System (NUCAPS) algorithm, developed at NOAA/NESDIS in cooperation with Goddard Space Flight Center (GSFC). Data are analyzed for open ocean areas with high vertical thermal contrast, defined here as the temperature difference between the surface and altitude of 4 km (Yurganov and Leifer, 2016a; Yurganov et al., 2016). CH_4 data are re-projected to a 4-km azimuthal equal area projection. The CH_4 anomaly (CH_4') is calculated by subtraction of the values computed within each of the 10 focus areas from the average of the whole Barents Sea for each year. As CH_4 shows high inter-annual variability, a three-year running average is applied. CH_4 retrievals are accurate over both ice and seawater.

Ocean *SST* are from the Moderate Resolution Imaging Spectroradiometer (MODIS) sensor on the Aqua satellite (NASA, 2015), obtained from the GSFC, Ocean Ecology Laboratory, Ocean Biology Processing Group (OEL-OBPG). The 4-km, Level 3 data are re-projected to a 4-km, equal azimuthal area projection. Satellite data products are cloud screened (Ackerman et al., 2010). The mapped products match the CH_4 data projection. Cloud filtering removes pixels with partial cloud coverage, which would change *SST*, from the dataset.

First, data are quality reviewed for sea ice coverage and cloud coverage filtered for coastlines, which are from the Global Self-consistent, Hierarchical, High-resolution Shoreline database (SEADAS, 2017). Shape files of sea-ice monthly extent are obtained from National Snow and Ice Data Center (Fetterer et al., 2017) and are based on monthly passive microwave radiometry with the Bootstrap algorithm (Comiso et al., 2008). Sea-ice fields are provided on a polar stereographic grid at 25-km resolution. The number of ice-free months is derived from the intersection of the monthly ice shape file for each year with the focus areas. The number of ice-free months each year is tallied by the following rules: if the intersection is less than 15%, it is counted as 0 months; if coverage is greater than 15% and less than 50% of the pixel, it is counted as 0.5 months. When coverage is greater than 50% in a single month the pixel is counted as ice covered for the month. Ice-covered (>50%) pixels are not used in the *SST* trend analysis and mean values.

The Cryosphere Discuss., https://doi.org/10.5194/tc-2018-237
Manuscript under review for journal The Cryosphere
Discussion started: 22 November 2018

2.2.2 Trend analysis

To estimate trends in the Barents Sea and adjacent areas, the monthly mean time series for each grid point in the images covering this region are calculated. Then, a first-order polynomial is calculated by linear regression analysis. Linear trends are analyzed using the Mann Kendall Test (Önöz and Bayazit, 2003) and Sen's linear trend analysis (Juahir et al., 2010; Sen, 1968).

Visual analysis of the trends and anomaly maps of the Barents Sea were used to determine the focus areas' locations. Trends for focus areas were calculated by averaging all valid (cloud cleared) pixels in each focus area for the same month for each year.

2.2.3 Focus Areas

The ten focus areas (**Fig. 4a; Table 1** for locations) are grouped into 5 oceanographic types. The north easterrly focus areas (A1-A3) characterize the inflow of Arctic surface water through both gaps between the archipelagos of Svalbard and Franz Josef Land and between Franz Josef Land and Novaya Zemlya. Each of these focus areas exhibits different seasonal ice coverage. Another group of focus areas is west of Spitsbergen (A4-A6) and is influenced by the West Spitsbergen Current and water from the Barents Sea. A focus area near Bear Island (A7) is affected by the warm, north-flowing NAC and the cold, southwest-flowing Bear Island Current (BIC) and thereby the closest to the Barents Sea Polar Front region (Harris et al., 1998). Three focus areas (A8, A9, and A10) were selected that are influenced by the Murman Current and MCC with focus area (A9) situated in coastal waters offshore southwest Novaya Zemlya with strongly, seasonally-varying ice coverage.

For the analysis, three sets of focus areas are chosen, "Northwest of Barents" including the Greenland Sea and Fram Strait, west of Spitsbergen (A4-A6), "Northern Barents" in the marginal ice zone at the edge of the Arctic Basin (A1-A3) and "Southern Barents," which is strongly influenced by heat from the east fork of the NAC (A7-A10). Of these, A8 and A10 cover banks and A7 covers a shelf, near Svalbard Bank. These groupings aare based on physical oceanography and exhibited similar trend patterns.

3.0 Results

3.1. Setting Overview

3.1.1. Barents Sea Oceanography and Meteorology

Currents are very important to Barents Sea oceanography (**Fig. 4**), dominated by inflow of warmer North Atlantic water through the North Atlantic Current (NAC), which forks into outflows along western Svalbard and through the Saint Anna Trough into the Arctic Ocean (Loeng et al., 1997). Cold Arctic water also flows into the Barents Sea through the Saint Anna Trough as the Percey Current (also Persey Current, PC). River inputs and flows between the Barents and Kara Seas are also important.

The relatively shallow (230-m average depth) Barents Sea is an adjacent sea to the Arctic Basin with complex bathymetry and hydrography (Loeng, 1991). The Barents Sea is bounded to the south by northern Europe and to the north by two archipelagos, Svalbard and Franz Josef Land (FJL). To the east lies the large north-south oriented, Novaya Zemlya archipelago, beyond which is the Kara Sea; to the west lies the Norwegian Sea. In winter the Barents Sea is partially ice-covered, while it is almost ice-free in the summer (**Fig. 4b**).

FIGURE 4 HERE – *Map of currents and focus areas in the Barents Sea*

The North Atlantic is a significant source of Arctic Basin water, whose density increases by cooling. Some of this water flows into the Barents Sea, ~2 Sv (1 Sv=10^6 m^3 s^{-1}), varying seasonally (Loeng et al., 1997) with most returning to the North Atlantic as part of the global thermohaline circulation (Aagaard and Carmack, 1989; Carmack and McLaughlin, 2011; Yamamoto-Kawai et al., 2008). McClimans and Nilsen (1993) used a laboratory simulation to duplicate most of the observed regional Barents Sea oceanographic features forced by the densities and volume fluxes of water from the Atlantic (the Norwegian Atlantic Current - NAC and the Norwegian Coastal Current - NCC) and Arctic Basin (Persey Current - PC) and Barents Sea hydrography. Key features were the general structure of fronts and major currents, etc., which were obtained without regional atmospheric forcing. This highlights the dominant importance of oceanography rather than meteorology to these features.

North Atlantic water flows through the Norwegian Sea, forming the NAC, one track of which becomes the West Spitsbergen Current (WSC), with the remainder flowing into the Barents Sea through the Barents Sea Opening as the North Cape Current (Piechura and Walczowski, 2009). The North Cape Current bifurcates into several forks mostly flowing to the east along the southern slope of the Barents Sea becoming the Murman Current (MC) near Murman.

The NAC is the major contributor of oceanic heat to the Barents Sea (Lien et al., 2017). Regional winds modulate the volume flow of Atlantic water into the Barents Sea–stronger in winter and weaker in summer (Stiansen et al., 2009; Fig. 2.3.4). Ice processes further complicate heat re-distribution for surface Arctic Ocean waters – ice insulates (better preserving its heat) the water from atmospheric radiative cooling. For example, the NAC's western fork (the WSC) submerges north of Spitsbergen (location varying seasonally) under an isolating layer of colder and fresher water furthering heat transport into the Arctic (Lien et al., 2017; Lien et al., 2013).

A south fork of the NAC is entrained into the NCC, which is 90% Atlantic water and 10% river discharge (Skagseth et al., 2008). The NCC is a major contributor of oceanic heat to much of the southern and eastern Barents Sea and into the Kara Sea (Lien et al., 2013). The NCC cools significantly through interaction with the atmosphere. Upon entering Russian waters, the NCC is renamed the Murman Coastal Current (MCC). Long-term (1905-) temperature data for the upper 200 m are available from a section off the Kola Peninsula (**Fig. 4a, Kola Section, black dashed line**), which the MCC crosses (Boitsov et al., 2012). These data reveal long-term trends with a cooler period from 1875-1930 and continuous warming of ~0.8°C since a minimum in 1970-1980 (Skagseth et al., 2008). The Kola Section data (which is full water column) show good gross agreement with long-term (since 1850) Barents Sea ice-extent (Walsh et al., 2016) – the warm period from 1930-1965 corresponds to a significant reduction of spring sea-ice (from ~0.2 to ~0.12). The Kola Section data shows steady warming since 1970 that corresponds to a consistent general sea-ice extent decrease since 1980 in spring and since 1970 in fall. This highlights that important long timescale forcing sed by the MCand MCC affects sea ice extent, meteorology, and oceanography in the southern and eastern Barents Sea.

Although beyond this study's scope, changes in the NAC/MC flow through the Kola Section relate to larger oceanographic trends. Skagseth et al. (2008) found good agreement in the Kola Section temperature trend with the Atlantic Multi-decadal Oscillation (AMO) index. *SST* lags atmospheric temperatures by 2-3 months, peaking for the Kola area (offshore Murman, Russia) between 0 and 200 m in September-October, whereas air temperature peaks in July (Stiansen et al., 2009, Figs. 2.3.3, 2.3.8).

The MCC continues eastward along the northern edge of the White Sea, becoming the Novaya Zemlya Current (NZC) until diverted northwards by Novaya Zemlya. It continues into the Arctic Basin through the Saint Anna Trough (SAT) between Franz Josef Land and Novaya Zemlya (Loeng, 1991), which is the dominant outflow of the Barents Sea (Maslowski et al., 2004). A fork of the MCC flows eastward into the Kara Sea through the narrow and shallow (20-50 m) Kara Strait (**Supp. Fig. S1** shows detailed Kara Sea currents).

A fork of the North Cape Current flows north through the Bear Island Channel towards the Hopen Deep (Loeng et al., 1997), underneath the cold, south-flowing Bear Island Current (BIC). Whitehead and Salzig (2001) suggested (and demonstrated in the laboratory) that remote forcing of the NAC through the Barents Sea lifts the current by several hundred meters to the sill of the Bear Island Channel, forcing significant anticyclonic vorticity. This drives the retrograde Bear Island Channel Current (BICC, our connotation) northeast along the slope of Svalbard Bank and the prograde Murman Current (MC) along the slope of Tromsøflaket, eastward and north to the east of the Central and Great Banks (Li and McClimans, 1998; Loeng, 1991). Li and McClimans (1998) referred to the BICC as the "Warm Core Jet" to emphasize its physical significance at the Polar Front. These merge east of the Central and Great Banks. The resulting flow cools from contact with the atmosphere into a denser, modified Atlantic Water flow that exits through the Saint Anna Trough to the east of Franz Joseph Land (Gammelsrød et al., 2009). Cooling at these banks also produces a dense westward underflow, depicted by the dashed line in **Fig. 4a**.

The Percey Current (sometimes spelled Persey, PC), transports cold, low saline, Arctic surface water into the Barents Sea to the east of Spitsbergen, becoming the Bear Island Current (BIC) to the west of the Grand Bank (**Supp. Fig. S2**). The Percey Current meets warmer, higher salinity waters of Atlantic origin in the Barents Sea, giving rise to the Barents Sea Polar Front (Oziel et al., 2016), whose location is controlled by seabed bathymetry, i.e., it is semi-stationary (Gawarkiewicz and Plueddemann, 1995). This front is part of a unique frontal system due to its combination with the seasonally ice-covered zones in the northern, central, and eastern Barents Sea (Vinje and Kvambekk, 1991). Part of the Percey Current merges with the East Spitsbergen Current (ESC) to the west of the Svalbard Bank and then flows north along the west Spitsbergen coast, inshore of the WSC, as the Spitsbergen Coastal Current (SCC). This flow loops the Barents Sea Polar Front around Spitsbergen (Svendsen et al., 2002).

Stratification plays an important role in the Barents Sea energy budget. Barents Sea water-column structure is modulated by winter cooling of surface waters and their convective mixing as well as brine rejection of seawater during ice formation. Winter vertical mixing extends to the seabed or near to the seabed over large portions of the shallow (200-300 m) Barents Sea (de Boyer Montégut et al., 2004). In spring, the warming of surface waters and freshwater from melting ice support water column stability and strengthens stratification in the central and southern Barents Sea (Loeng, 1991). Stratification isolates deeper waters from the atmosphere, preventing heat exchange with the atmosphere and the vertical mixing that traps dissolved CH_4 in deeper water (Leifer et al., 2015). Coastal waters off Norway and Murman remain stratified year-round due to terrestrial freshwater inputs (Loeng, 1991).

Eastern Barents Sea winds generally circulate counterclockwise (cyclonically), strongly to the north along Novaya Zemlya in winter and weakly to the south in summer and fall (Gammelsrød et al., 2009). This leads to calm winds over the Central Bank in fall and winter and generally weak easterlies near Franz Josef Land (fall to spring). Near Spitsbergen, winds are from the north year-round, weak in summer and strong in winter (Kolstad, 2008; Moore, 2013). The spring wind pattern is similar during winter, albeit displaced southwards and weaker. In summer, moderate winds (6 m s^{-1} average) blow from the north over most of the Barents Sea. Fall winds are similar to the summer, but stronger (~8-10 m s^{-1}) in the west (near Spitsbergen) and weaker in the east near Novaya Zemlya. Summer south Barents Sea winds are towards the north and later east near coastal Norway and Murman. The Barents Sea is stormy–winds are above 15 m s^{-1} for over 125 days per year, mostly from the south (Kolstad, 2008). Thus, in the east Barents Sea, winter winds transport more southerly, potentially warmer air, and in the summer winds from the southwest can transport warmer air along Norway and from the west along the Murman coasts; however, most of the Barents Sea most of the year experiences cold northerly winds. Moreover, much of the winter eastern Barents Sea is ice covered, insulating the sea from the air.

Air temperatures on Bear Island have risen ~1.7°C since 1980 (Boitsov et al., 2012), about triple the global atmospheric trend over the same period of ~0.6°C (http://eca.knmi.nl/) and about double the overall Arctic average (Hoegh-Guldberg and Bruno, 2010). For reference, temperatures in Murman have risen far faster at 0.12°C yr^{-1} and 0.11°C yr^{-1} in June and September 2002-2017, respectively (**Supp. Fig. S4**). These differences reflect that Bear Island is embedded in the marine rather than the coastal atmosphere and is influenced by the cold Bear Island Current.

3.1.2. Kara Sea Oceanography and Meteorology

Kara Sea hydrography is controlled by the freshwater outflow of the Ob and Yenisei Rivers (**Fig. 2b; Supp. Fig. S1 for finer details**), which contribute 350 and 650 km^3 yr^{-1}, respectively (Stedmon et al., 2011), approximately double that of the Mississippi River, primarily (>75%) between May and September. As a result, the eastern Kara Sea is brackish. Riverine sediment leads to the northeast Kara Sea being mostly shallow (< 50 m). The western Kara Sea is deep (mostly >100 m), descending to below 500 m in the Novaya Zemlya Trough (Polyak et al., 2002).

Deeper water in the trough is supplied by inflow of modified Atlantic water from the northern Barents Sea into the deep Novaya Zemlya Trough. Trough water is dense and fully saline. On the surface, inflows to the north Kara Sea come from the MCC, local runoff, and ice supplying the Novaya Zemlya Coastal Current (NZCC), with some flow returning to the Barents Sea through the Kara Strait. Warmer water enters the south Kara Sea from the Barents Sea as the MCC flows through the Kara Strait, joining a northward flowing slope current. Much of this water mixes with the southern flowing NZCC and returns to the Barents Sea through the Kara Strait (McClimans et al., 1999; McClimans et al., 2000, Secction 11). River outflow drives the overall Kara Sea surface currents largely northwards. Prevailing winds are mostly from the southwest for the western Kara Sea and from the south to southwest in the

The Cryosphere Discuss., https://doi.org/10.5194/tc-2018-237
Manuscript under review for journal The Cryosphere
Discussion started: 22 November 2018

central Kara Sea (Kubryakov et al., 2016). Much of the Kara Sea (particularly north) is ice-covered in July and mostly ice-free by September.

3.2. Barents Sea *In situ* Observations

In situ CH_4 measurements were made by cavity enhanced absorption spectroscopy (Los Gatos Research Inc., Mountainview, CA). Both transits followed a very similar trajectory (**Supp. Fig. S5b**) that passed through focus areas A1 and A2. Very large, localized, CH_4 anomalies were observed, including in focus area A2 (**Fig. 5**; **Supp. Fig. S5b** shows the full dataset). These anomalies were far offshore, indicative of local (i.e., marine) not distant (i.e., terrestrial) sources. The only reasonable explanation is seep bubble plumes – vessel exhaust was ruled out - see **Supp. Sect. S5** for more details.

FIGURE 5 HERE – *In situ methane data*

There was an abrupt decrease in CH_4 around 72°N for the outwards transit, which increased again around 75°N. This depressed CH_4 portion of the transit was near where the vessel left the warm Murman Coastal Current (**Supp. Fig. S4b**). The strongest anomaly, to 2000 ppb, was observed on the southwards transit where the MCC rises over the sill into the Saint Anna Trough (78.7°N), close to the focus area 8 (**Fig. 5)**.

The two transits were separated by about a month with the September transit higher by ~30 ppb than in August, consistent with strong seasonal CH_4 changes. There were other significant differences. Whereas several narrow (and thus local) CH_4 anomalies were observed during the southwards transit, orders of magnitude more narrow anomalies were observed during the northwards transit. Also, the significant peak at 78.7°N only was observed during the southwards transit, indicating emissions variability.

The difference between these transits highlights the challenges of interpreting such snapshot data, supported by the comparison with IASI pixels that were proximal and within several days (**Supp. Fig. S6**). Agreement for the northwards transit was reasonably good (generally within 10 ppb), and generally poor for the southwards transit.

3.3. Focused Study Area Annual Trends

Focus areas with the strongest decreasing ice cover trends from 2003-2015 are in the marginal ice zone of the northern Barents Sea (south and southwest of Franz Josef Land) at the southern margin of the Arctic Basin (**Fig. 6a**, **A1-A3**). Trends for these three study areas are very similar (after classifying 2006 and 2014 for focus area A4 (Spitsbergen Northwest) as outliers. Note, focus areas A1-A3 show below-trend ice-free months in 2014 despite no significant 2014 *SST* deviation, supporting its classification as an outlier (**Fig. 7a**).

FIGURE 6 HERE – focus area ice-free trends

The similarity in ice coverage trends for area A3 (along the cold Percey Current) with areas A1 and A2 (along the Murman Current's warm, northward leg) suggests not only increasing northward heat transfer, but also

The Cryosphere Discuss., https://doi.org/10.5194/tc-2018-237
Manuscript under review for journal The Cryosphere
Discussion started: 22 November 2018

weakening southward cold-water advection. Area A4 (northwest of Spitsbergen) also shows decreasing ice coverage towards more frequent year-round ice-free status and lies at the Arctic Basin boundary (**Fig. 6b**), albeit more under the influence of warmer NAC waters than those under the influence of the Murman Current in the north-central Barents Sea (A1-A3). The Central Bank of the Barents Sea (**Fig. 6c, A10**) last saw an ice-covered month in 2005, while a noisy trend of decreasing ice coverage is evident offshore coastal southwest Novaya Zemlya (**Fig. 6c**, **B9**), along the western fork of the Murman Coastal Current.

Overall, all focus areas are trending towards year-round ice-free, with the entire Barents Sea likely to be year round ice free by ~2030 based on an extrapolation of trends in Northern Barents Sea focus areas, A1-A3.

FIGURE 7 HERE - – focus area SST trends

SST increases in all focus areas, albeit at rates spanning a wide range from 0.0018 to 0.15 °C yr^{-1} (**Fig. 7; Table 1**). In the Northern Barents Sea, the strongest warming trend is for area A1, south of Franz Josef Land. This is located in a marginal ice zone in the path of the warm MC. Area A3 shows the weakest warming trend lies along the cold Percey Current. For the Northwest of Barents focus areas (**Fig. 7b, A4-A6**), the strongest warming is at the northernmost focus area, A4, whereas the weakest trend is for the southernmost focus area (**Fig. 7, A6**). This is consistent with a strengthened northwards penetration of the warm NAC and thus both the West Spitsbergen Current (WSC) and Bear Island Channel Current (BICC).

The strongest warming trend occurs southwest of Novaya Zemlya (**Fig. 7c**, **A9**) along the path of the northerly turn of the MCC, in shallow water. This trend is consistent with increased eastward MCC penetration east along the coast of Novaya Zemlya and into the Kara Sea. A very weak and highly variable *SST* warming trend is observed to the south of the Svalbard Bank at the intersection of the cold Percey Current with the warm NAC and BICC (A7). Areas A10 and A8, and to a lesser extent A9 all suggest a strong oscillation of ~8 years with peak values in 2005 – 2007, and a minimum around 2010. The same pattern also is observed to the south of Franz Josef Land (areas A1 and A2). All the boxes that exhibit this variability lie along the Murman Current, whose origin is in the NAC.

FIGURE 8 HERE – *Focus area methane trends*

A positive CH_4' trend is observed across the Barents and Kara Seas from June through September with some regions exhibiting far stronger trends than average (**Supp. Fig. S7**). Areas of faster CH_4' increase include near Franz Josef Land (**Fig. 8a**, **A1**, **A2**), the shallower waters offshore W. Spitsbergen (**Fig. 8b**, **A4**), and offshore Novaya Zemlya (**Fig. 8c**, **A9**). These areas of increasing CH_4' correspond to areas of consistent warming for 2003-2015 (**Fig. 7a**, **A1, A2**) and consistent warming since ~2004/2005 for southwest offshore Novaya Zemlya and the Central Bank of the Barents Sea (**Fig. 7c**, **A8-A10**). All these focus areas lie along the northwards flow of the Murman Current and the Murman Coastal Current. The Central Bank also gets heat inflow from the BICC "warm core jet." Focus area A2 was crossed by the *in situ* transit and found CH_4 anomalies (Fig. 5c) best explained by CH_4 seepage. In

The Cryosphere Discuss., https://doi.org/10.5194/tc-2018-237
Manuscript under review for journal The Cryosphere
Discussion started: 22 November 2018

The Cryosphere Discussions
Open Access
EGU

contrast, focus areas along the Percey Current show a slowly decreasing CH_4' defined as relative to the entire Barents Sea trend (**Fig. 8**, **A3, A7**), despite an (albeit weakly) increasing *SST*.

The strongest CH_4 growth is south of Franz Josef Land (**Table 1 A2**, 3.49 ppb yr^{-1}), followed by offshore northwest Spitsbergen (**Table 1 A4**, 3.37 ppb yr^{-1}- 2003-2015, 3.6 ppb yr^{-1} 2005-2015). This positive trend is sustained over the analysis period. The area off the Fram Strait has natural CH_4 seepage associated with hydrate destabilization (Westbrook et al., 2008). This is an annual increase, and thus does not result from shifts in the timing of seasonal warming. Note, the CH_4' slopes for areas A4-A10 all are larger when calculated from the 2005 minimum, but not for A1-A3 (**Table 1**). The former lie along the NAC and its eastern current fork, the Murman Current. Neither the Percey Current focus areas (A3, A7) nor other northern Barents Sea focus areas (A1, A2) show this effect depending on the reference time.

TABLE 1 HERE

The largest variability in *SST* and CH_4' was in the focus area to the north of Murman in the Murman Current (MC) (**Table 1, A8**; **Fig. 8**) which could arise from variations in the strength of the MC – Skagseth et al. (2008) shows nearly 50% variability in the volume flux through the Barents Sea Opening flux on decadal time-scales. Additional variability occurs from meteorology (and resultant change in cloudiness and hence solar insolation/downwelling radiation), and shifts in the location of the MC, which bifurcates around the focus area.

In general, CH_4' was at a low for most of the northwest Barents and southern Barents sites for the period 2004-2006 with an approximately 6-8 year cycle. Boitsov et al. (2012) shows variability in the seabed temperature for 2000-2009 suggesting a period of ~5-7 years, with the coolest seabed temperatures 2002-2005. This suggests a multiyear delay between changes in seabed temperatures and changes in CH_4 emissions, likely related to timescales for heat transfer through overlying sediments.

3.4. Climatology of the Barents and Kara Seas

Atlantic heat input is very important to the energy budget of the Arctic Basin and Barents Sea and is driven by the two forks of the NAC (**Fig. 4a**) (Lien et al., 2013). In addition to meteorological forcing and radiative balance, currents significantly affect *SST*. This importance is evident in the Barents Sea *SST* climatology where warm *SST* follows the path of the warm currents (**Fig. 9; Supp. Fig. S3**). Warmer water flows eastward along the northern Norwegian and Murman coasts and offshore southeast of Spitsbergen along Svalbard Bank and then northward along the western Spitsbergen coast. In June, these flows correspond to “tendrils” of warmer water extending north to the east of the Central Bank and to the west of Novaya Zemlya and around Bear Island (**Supp. Fig. S3a**) and in September in the east Barents Sea (**Supp. Fig. S3b**). Water becomes cooler as it penetrates eastward, and as it reaches the (seasonally-varying) ice edge (**Supp. Fig. S3**). Across much of the Barents Sea there is a strong latitudinal *SST* gradient extending south from the ice edge, independent of the location of the eastern NAC branches. In the coastal waters of Novaya Zemlya, warmer water extends further north than elsewhere. The warm signature disappears in the area where the NAC submerges, near northwestern Novaya Zemlya (**Fig. 4a**).

FIGURE 9 HERE – *Maps of Mean values of SST and CH4 for BKS*

In June, the edge of the cold (Arctic water) Percey Current/Bear Island Current corresponds well with the warm water's edge and also corresponds fairly well with the median ice edge location. Southeast of Spitsbergen, the Bear Island Current penetrates southward as a narrow extension of cold water ending south of Bear Island. Slightly cooler water is observed over the two banks in the central Barents Sea.

The shift to summer *SST* patterns occurs in July, increasing in August, and then beginning to decrease in September (**Supp. Fig. S6**). For Spitsbergen in the Svalbard archipelago (**Supp. Fig. S2**) the northerly cold Spitsbergen Coastal Current (SCC) inshore of the West Spitsbergen Current (WSC) breaks down. This suggests the SCC is entrained by the more energetic WSC (McClimans, 1994), flowing northwards underneath colder surface winds along southwest Spitsbergen, likely below strong summer stratification. The WSC flows farther offshore in June than in September, i.e., the Barents Front shifts shoreward in summer (**Supp. Fig. S3**).

September *SST* in the shallower eastern (coastal) Barents Sea has warmed to levels comparable to the warmer waters in the southwest Barents Sea where NAC heat input maintains elevated *SST*. Warmer *SST* also extends further offshore Norway and Murman. These seasonal *SST* changes match the sea ice's northwards retreat to Franz Josef Land (**Fig. 9b**) and shift of coastal winds to tailwinds over the currents (**Supp. Fig. S3**). However, Barents Sea warming does not follow the ice edge between Svalbard and Franz Josef Land, corresponding instead to the front of the cold Percey Current. From August to September, the warm water has begun retreating across the Barents Sea with cold water associated with the Percey Current (**Supp. Fig. S7**).

The now mostly ice-free Kara Sea in September exhibits coastal warming, particularly to the east, where there also is heat input from the Ob and Yenisei Rivers (east of the Yamal Peninsula). This area exhibits warming despite partial ice coverage of the Gulf of Ob in June and likely is driven by warmer riverine water inputs.

CH_4 concentrations show a clear latitudinal trend that increases towards the north. This latitudinal gradient is weak in June and strong in September. Strong localized variations also occur in different Barents Sea regions. CH_4 concentrations along the Murman Current and in the (ice-covered) Kara Sea largely are below the latitudinal mean in June, whereas west of Spitsbergen and in the north-central Barents Sea they are above average.

In June, CH_4 is depressed strongly around Svalbard and around Franz Josef Land and Novaya Zemlya. For Spitsbergen, this corresponds to the SCC that hugs the shore. By September, CH_4 concentrations are notably different with significantly higher CH_4 and a distinctly different spatial distribution. Most notable is the shift from depressed to strongly enhanced CH_4 in the region to the west of Novaya Zemlya, particularly the Novaya Zemlya Bank, and around the Franz Josef Land archipelago. Strong CH_4 enhancement also occurs in the outflow plumes of the Ob and Yenisei Rivers in the Kara Sea, around the Taymyr Peninsula. Around Svalbard, CH_4 has risen to near latitudinal mean levels in September, except for offshore north Spitsbergen and Nordaustlandet, where sea ice remains.

3.5. Barents and Kara Seas Trends

Across the Barents Sea, a number of different focus areas with distinct *SST* and CH_4' trends are identified (**Fig. 7**). These manifest significant spatial heterogeneity at the pixel scale and at the focus-area size scale. We apply our analysis to aggregated-pixel "focus areas" located in key regions where *SST* temporal and spatial changes are strongest (**Sec. 3.3**; **Supp. Fig. S8** for July and August trends).

June *SST* warming trends (*dSST*/*dt*) are fairly different from September *SST* trends (**Fig. 10**). In June, warming occurs much faster in the eastern Barents Sea, specifically, in waters affected by the Murman Coastal Current (MCC). Given that winds are from the north (**Supp. Fig. S3**) current-mediated heat transport opposes current warming. This suggests the magnitude of atmospheric cooling during transit from the Atlantic is decreasing. Warming occurs primarily in shallow (generally less than 100-m deep) (**Fig. 10b**) waters that are generally well mixed. Sea ice is absent in this region by March-May, later in more northerly areas (**Fig. 4b**). Whereas there is no clear warming trend in July and August; a strong warming appears in the Kara Sea by September (**Supp. Fig. S8**), where winds also are cold northerlies. That this warming occurs several months after the ice retreat suggests that insolation is less important after the ice melts – the Kara Sea is ice-free in July (**Supp. Fig. S7**). This is consistent with increasing MCC penetration into the Kara Sea. Loeng (1991) reported that MCC penetration into the Kara Sea was uncommon in the middle of the 20th century.

FIGURE 10 – *Maps of trend values of SST and CH4 for BKS*

More rapid warming occurs offshore of the western coast of Novaya Zemlya from June-September. This is where the Murman Current (MC) transports water towards the St Anna Trough (the dominant Barents Sea outflow), a region where shoaling is likely based on seabed topography (**Fig. 2b**) (Maslowski et al., 2004). The MC then flows (and submerges under ice and Arctic surface water) along the east shores of Franz Josef Land. Accelerated warming diminishes near the northern margin of the Kara Sea, where river outflow dominates the oceanography.

Enhanced warming also occurs to the south and to the west-northwest of Svalbard in September, following approximately the trend of the northerly fork of the NAC. In contrast, waters off east Svalbard, where the East Spitsbergen Current (ESC) transports cold Arctic waters southwards, do not exhibit a significant warming trend in September, although it does exhibit warming in July. This suggests changes in the seasonal penetration of the PC into the Barents Sea, likely modulated by seasonal ice sheet retreat. There is no significant *SST* warming in June or September to the north of Franz Josef Land with ice-coverage persisting through September.

Overall Barents Sea atmospheric CH_4 is increasing (**Fig. 9C**), consistent with the global CH_4 trend (Nisbet et al., 2014). However it is notable that some regions exhibit significantly more rapidly increasing CH_4' than the global or Barents Sea trends. In June, CH_4 trends are largely similar in both ice-free and ice-covered areas. In near-coastal waters around Svalbard (except the east), in northern Norwegian fjords, and for the White Sea (Murmansk) where CH_4 growth is enhanced.

September CH_4' trends (dCH_4'/dt), when ice coverage has retreated to the northern edge of the Barents and Kara Seas (**Fig. 9b**), are strongly enhanced in the east Barents Sea and the south Kara Sea. These areas coincide with areas of enhanced *SST* warming and show CH_4' trends almost three times as high as the general Arctic trend. Moreover, they are under northerly winds and thus terrestrial sources cannot contribute (**Supp. Fig. S3**). In contrast, regions without enhanced warming, particularly waters affected by cold currents, exhibit the weakest CH_4' growth; slightly above the rate of overall Barents Sea growth. Also, CH_4' increases strongly In the Kara Strait between the Barents and Kara Seas.

Enhanced CH_4' growth is not evident in June or September to the north of Spitsbergen, despite strong *SST* increases; however, significant increases are evident here in August. This follows significant CH_4 enhancement in July to the southeast of Spitsbergen. This July-August shift follows the NAC.

4. Discussion

In this study, we test the hypothesis that CH_4 in the lower troposphere correlates with changes in overall water column temperature, which are reflected in *SST* trends. Specifically, the presence of increasing CH_4 emissions where *SST* is increasing implies that the *SST* trend is not a surface skin effect, but increasing water column temperature. Both *SST* and CH_4 are satellite remote sensing products

The proposed source of the atmospheric CH_4 anomaly is seabed seepage (**Section 4.2**) from either thermogenic sources, i.e., petroleum hydrocarbon reservoirs (Judd and Hovland, 2007), or degradation of submerged permafrost and hydrates (Shakhova et al., 2017). Both permafrost and hydrate deposits can include both thermogenic and biogenic CH_4. Submerged permafrost likely is extensive in the east Kara Sea and potentially in the southeast Barents Sea (**Fig. 2**) (Osterkamp, 2010). Pockmark fields, typically associated with CH_4 seepage, have been mapped in the central northern Barents Sea (Lammers et al., 1995; Solheim and ElverhøI, 1985) and southwest Barents Sea (Rise et al., 2015) and near Franz Josef Land (Sokolov et al., 2017), including water-column CH_4 plumes.

For this analysis, we also considered the locations of currents and trends in these currents, seabed bathymetry, prevailing winds, and available Barents Sea, water-column temperature data–primarily the long-term Kola Section data, which due to the importance of the Murman Current is directly relevant (Boitsov et al., 2012), as well as meteorology data in coastal Murman (**Supp. Fig. S4**). We test the methane-shoaling hypothesis (**Section 4.3**) – that currents drive deep methane to shallower waters where it can transfer into the atmosphere distant from its seabed source.

4.1. Seabed-atmosphere methane transport

There are a number of mechanisms that allow seabed CH_4 emissions to reach the sea surface, both due to direct bubble-mediated transport and by turbulence (from bubble-dissolved CH_4). Transport is bubble-mediated (Judd and Hovland, 2007), because the microbial filter generally reduces aqueous CH_4 as it migrates through sediments into the water column (Reeburgh, 2003). As a bubble rises, it loses CH_4 to the water column by dissolution, transporting the remainder. Larger bubbles lose less gas than smaller bubbles – rising higher in the water column (Leifer and Patro, 2002). In shallow water (e.g., less than 20 m), most seep bubble CH_4 reaches the sea surface directly, with the fraction decreasing for smaller bubbles or deeper (Leifer and Patro, 2002). For example, Leifer et al. (2017) showed that ~25% of seabed CH_4 from 70 m reaches the Laptev Sea surface directly, consistent with sonar observations of seep bubble plumes reaching the sea surface (Leifer et al., 2017). Some of the dissolved fraction is transported vertically by the bubble-driven upwelling flow (Leifer et al., 2009), even for small plumes (Leifer, 2010). CH_4 deposited within the WWML diffuses rapidly to the atmosphere, although seasonal stratification powerfully suppresses this transport. Storms breakdown this stratification (Leifer et al., 2015) sparging all the dissolved CH_4 to the atmosphere (Shakhova et al., 2013). Seasonally, the collapse of the pycnocline from fall storms releases CH_4 temporarily sequestered in the deep WWML (Nauw et al., 2015). Although some of the dissolved CH_4 in the WWML will be oxidized microbially turbulence transport in stormy arctic seas is efficient. In practical terms, bubble transport means that seepage extends the effective WWML depth for CH_4 by 50-100 m, i.e., 150-300 m, allowing wave turbulence and storms to sparge dissolved CH_4 to the atmosphere over most of the Barents and Kara Seas (**Fig. 2b**).

Below the winter wave mixed layer (WWML), oceanic microbial oxidation timescales are shorter than transport timescales and all dissolved CH_4 likely is oxidized (Rehder et al., 1999). Still, CH_4 below the pycnocline may drift with currents that drive it upslope into the WML where it can escape to the atmosphere, possibly distant from its seabed origin - methane shoaling. Even for the worst case, CH_4 microbial oxidation timescales in plumes are several weeks (Reeburgh, 2007), over which currents can transport CH_4 order 100-1000 kilometers. Outside of plumes, oxidation timescales are much significantly longer–decades for deepsea background concentrations (Reeburgh, 2007).Methane shoaling also enhances transport of shallower dissolved CH_4 to the atmosphere.

The above discussion was for non-oily seepage. However, where seepage arises from a petroleum hydrocarbon reservoir, bubbles likely are oily. Oil slows bubble rise (Leifer, 2010) and dramatically reduces dissolution, allowing their survival far higher in the water column than non-oily bubbles (Leifer and MacDonald, 2003). Oily bubbles can reach the sea surface from the deep sea – e.g., MacDonald et al. (2010) tracked seep bubbles by remote operated vehicle from 1 km depth to the WML and found a significant positive CH_4 anomaly in surface waters. Given the presence of extensive proven and proposed petroleum reservoirs across the Barents and Kara Seas (Rekacewicz, 2005), some Barents Sea seepage is likely oily with enhanced CH_4 transport to the sea surface. The *in situ* data (**Fig. 5**) showed localized strong atmospheric CH_4 plumes above deep water that are best explained by oily bubbles. These plumes were above areas of confirmed oil and gas deposits within an extensive region of potential oil and gas deposits in the central and northern Barents Sea (**Supp. Fig. S9**). Thus, the *in situ* data suggest more extensive oil deposits than currently confirmed deposits. Observations of oil slicks would provide confirmation, but require calm winds.

One unlikely source of CH_4 anomalies for the Barents and Kara Seas is atmospheric transport as there is neither significant local industry nor extensive wetlands/terrestrial permafrost nearby or upwind for the prevailing wind directions. Prevailing winds are from the north in June and September except for south and southeast Barents Sea where winds track the coast and NCC and MCC in September (**Supp. Fig. S3**). Note–synoptic systems can transport CH_4 from northern Europe or Russia to the Barents Sea, but synoptic system winds are not dominant (prevailing) and thus play a small role in time-averaged datasets. Moreover, these terrestrial sources are distant, implying large size scale anomalies, which would decrease with distance from northern Europe. Instead, the anomalies are localized and decrease towards Europe, and the *in situ* data (**Fig. 5**) show highly localized anomalies. The one area where September winds could transport terrestrial CH_4 into the marine atmosphere is from oil production and pipeline infrastructure from the Kanin and Yamal Peninsulas near Kolguyev Island (**Supp. Fig. S9**). However, extensive CH_4 plumes (**Figs. 9 and 10**) are not observed in coastal pixels, and dCH_4/dt trends were not lower than those further offshore. This is consistent with the general trend of decreasing Russian CH_4 emissions from conventional oil production (Höglund-Isaksson, 2017).

4.2. Hydrocarbon Reserves and Local Atmospheric Methane

Seabed seepage, often thermogenic (petroleum hydrocarbon), has been identified in all oceans and all petroleum-producing basins (Judd and Hovland, 2007) and likely plays a role in CH_4 anomalies in the Barents and Kara Seas.

In the Kara Sea, the correlation of enhanced CH_4 with depth is poor, which is shallower to the north. Instead, the location of enhanced September CH_4 closely matches the location of oil and gas reserves, e.g., **Supp. Fig. S9;** Rekacewicz (2005), and also the Murman Coastal Current's path of warm water as it follows the coastline of the Kanin Peninsula and then enters the Kara Sea. Although there is extensive oil and gas production on the Yamal Peninsula, prevailing winds blow away from the Barents Sea. Note, the trend shows enhanced CH_4 growth, implying increasing emissions, i.e., not steady-state seabed warming but increased seabed warming. This increasing CH_4 growth is for September, not June, corresponding to when the water column is warmest in the South Barents Sea (Stiansen et al., 2009). Also, the Barents Sea outflow through Saint Anna's Trough is greater in September (about double) than June (Gammelsrød et al., 2009) when the growth in the CH_4 anomaly occurs (**Fig. 10d**). The importance of this transport also is apparent in the *SST* trend with the greatest warming occurring in June in the southeast Barents Sea (offshore the Kanin Peninsula) near the Kara Strait. This region lies to the west of the areas of enhanced CH_4 growth in September near the Kara Strait. In contrast, significant *SST* warming is not observed in September in this easternmost region of the Barents Sea.

Two other areas of enhanced CH_4 growth lie in the north-central Barents Sea, north of Central Bank, and offshore northern Novaya Zemlya. These regions lie along the Murman Current and over the Central Bank – a region where the MC and the BICC "warm core jet" converge. Water flowing in this direction also is forced upwards – from 300-400 m to just 100 m as it crosses a sill into the St. Anna Trough with rising seabed towards the east and towards Novaya Zemlya with water depths of just tens of meters (**Fig. 2B**). Additionally, this region of increasing CH_4 growth corresponds spatially to the potential (i.e., unproven) gas and oil reserves that extend across the Saint Anna Trough to Franz Josef Land, e.g., **Supp. Fig. S9**; Rekacewicz (2005). There also are proven oil and gas fields to the south, also along the Murman Current's path, but south of the area of increasing CH_4 offshore northwest Novaya Zemlya. These hydrocarbon fields also correlate with increasing CH_4 trends offshore southwest Novaya Zemlya.

4.3. Methane Shoaling Hypothesis

Where CH_4-rich currents shoal, they vertically transport dissolved CH_4 into shallow waters where it can diffuse to the atmosphere. This process, termed *methane shoaling*, allows seabed CH_4 to reach the atmosphere distant from its seabed source, often beyond the reach of *in situ* studies. In this study, the global and continuous view of satellite data allowed investigation of the methane-shoaling hypothesis.

In general, if seabed CH_4 seepage is sufficiently deep and below the WWML and non-oily, its direct atmospheric contribution is small to none. Even plume microbial oxidation CH_4 rates of several weeks (Reeburgh, 2007) allows significant horizontal transport by currents – note, timescales increase to decadal for typical deepsea concentrations (Rehder et al., 1999). Where currents force these waters upslope, CH_4-rich waters are brought to shallower depths where mixing allows sea-air transport into the atmosphere. *Shoaling of methane-laden water* provides the best explanation for the localized, strong and growing, atmospheric CH_4 anomalies in the Barents and Kara Seas, specifically the Kara Straits and along the Novaya Zemlya coast near Central Bank and elsewhere.

Areas of enhanced CH_4 growth were closely related to the path of the Murman Coastal Current as it flows towards the Kara Strait rather than seabed depth (**Fig. 10**). Both the rising seabed bathymetry and the presence of both southwards and northwards currents through the Kara Strait imply strong vertical mixing and thus transport to the atmosphere. Along the path of the Murman Current are significant offshore petroleum hydrocarbon reservoirs that likely release seep CH_4 into the waters of the Murman Current.

Further evidence that transport and methane shoaling is important is from the dCH_4/dt spatial distribution around Kolguyev Island (north of the White Sea), which is increasing faster on its western side than its eastern side, even though the seabed to the island's east is shallower. In fact the CH_4 spatial pattern correlates better with shadowing in the island's lee from shoaling currents, rather than with seabed depth. Prevailing winds are from the south-southeast (Kubryakov et al., 2016), thus atmospheric transport cannot explain the pattern.

Notably, the enhanced CH_4 concentrations around Franz Josef Land does not correlate with the potential reserves, but does correlate with depth and the flow of the Murman Current, consistent with methane shoaling. Although some of the enhanced CH_4 growth near Novaya Zemlya could arise from increasing local seabed emissions, seabed temperatures were below zero until 2009 (Boitsov et al., 2012), which would imply submerged hydrate deposits here have not yet degraded significantly, supporting the methane shoaling mechanism.

4.4. Sea Surface Temperature

The analysis not only shows spatial anomalies that likely result from a combination of local sources - likely thermogenic seepage – and methane shoaling, but also shows CH_4 anomaly growth (dCH_4/dt) that implies strengthening seabed sources if atmospheric conditions remain constant. Specifically, dCH_4/dt over *portions* of the Barents and Kara Seas is faster than the Barents Sea mean and the latitudinal mean. To some level these correlate with enhanced *SST* warming, but the correlation is poor. *SST* is the skin temperature and depends on radiative balance, atmospheric temperature (including transport and latent heat) and heat transfer from the bulk ocean. Another factor underlying this poor correlation is that there is a delay between *SST* warming and ocean-column warming of several months (Stiansen et al., 2009). There also appears to be a several year response time; the ~6-8 year variability is suggestive of an oscillation in the *SST* trend in the Southern Barents Sea (areas A8, A9, and A10) and has a very similar timescale to the seabed trends reported by Boitsov et al. (2012), albeit preceding it by ~2-4 years.

More rapid *SST* warming occurs offshore Novaya Zemlya moving northwards from June-September, where the Murman Current transports water and the seabed topography is likely to cause shoaling. This suggests that warmer terrestrial weather is not driving Kara Sea changes as this would occur uniformly both in the south Kara Sea, which is influenced by the Barents Sea, and the northern Kara Sea, which is influenced by river outflow. Additionally, if increased riverine heat input were driving the trend, the greatest enhancement would be in the northern Kara Sea, which also is shallower.

There are a number of possible hypotheses for why *SST* is warming fastest in waters along the Murman Current and NAC. One is sea-ice retreat; however, the warming occurs several months after the retreat of the sea ice. Another is that the mixed layer is becoming shallower, allowing more rapid cooling to the atmosphere. This would imply a weakening of storms and winds – which firstly is inconsistent with warmer *SST*, and secondly, there is no indication that Barents Sea storminess is changing or progressing further northwards (Koyama et al., 2017). Cloudiness changes affect *SST*; however, cloud filtering at the pixel level removes this effect from the analysis, whereas persistent cloudiness changes largely cancel outside of areas of sea ice retreat (Schweiger et al., 2008).

Another hypothesis is that increasing ocean current heat transport is driving the *SST* warming. Although *SST* derives from several factors including heat transfer from the bulk ocean (i.e., currents), its co-spatial relationship to enhanced CH_4 anomaly is consistent with currents playing a major role both at the sea surface (*SST* anomaly trend) and at the seabed. This supports using *SST* as a surrogate for water column temperature. Greater heat transport could occur from strengthening currents, or warming currents, or a combination of both.

Seabed September temperatures (Boitsov et al., 2012) do not suggest increased warmer seabed temperatures north of Norway and Russia, but do suggest warmer seabed temperatures to the east and also along Novaya Zemlya – suggesting a greater importance of the MC. This is consistent with the model of McClimans et al. (2000) that currents are advecting ice, shifting the marginal ice zone location. The warming trend suggests a strengthening of the seasonal trend in the Barents Sea outflow, which is greater in September than June (Gammelsrød et al., 2009).

The most rapid warming is for the shallow water off northwest Svalbard (area A4) (**Fig. 10b**), which also exhibited the strongest CH_4 growth. In this area, seabed topography is nearly flat over an extensive shelf with depths in the range 250-400 m. Where the shelf falls off sharply, rising sea temperatures will minimally induce hydrate destabilization. In contrast, where the shelf falls off very gently, small temperature increases shift extensive areas of seabed from below to above the hydrate stability field. This area is immediately to the north of the area where several researchers have identified extensive seabed seep CH_4 emissions (Mau et al., 2017; Myhre et al., 2016; Westbrook et al., 2009). The most likely explanation is a strengthening of the West Spitsbergen Current, discussed below, and shifts in the Barents Sea Polar Front.

4.5. Implications for Svalbard Area Methane Emissions

There are few atmospheric and ocean CH_4 data for the Barents Sea and surrounding areas, the most prominent being associated with CH_4 seepage off Spitsbergen, located immediately south of focus area A4. Studies to date have been in early summer; Mau et al. (2017); Myhre et al. (2016) who made measurements in the atmosphere and water column while Westbrook et al. (2009) reported sonar observations of seep bubbles for August-September, and slightly elevated aqueous CH_4 in surface waters immediately above the bubble plumes. All concluded transport to the atmosphere was not significant, attributed to trapping of dissolved CH_4 below a sharp pycnocline. It is important to note that with respect to the overall Barents Sea area CH_4 anomaly, the Svalbard area is far less important than around Franz Josef Land, off the west coast of Novaya Zemlya, and the north-central Barents Sea (**Fig. 9**).

Both *SST* and CH_4 in June (**Fig. 9**) and July (**Supp. Fig. S7**) for west Spitsbergen show that much of the area of active seepage was inshore of the Barents Sea Polar Front, and thus under the cooling Arctic waters of the Spitsbergen Coastal Current (SCC), supported by reported salinity data (Mau et al., 2017). Although *SST* remains suppressed off Spitsbergen in September, and extends further offshore, CH_4 concentrations no longer are depressed compared to Atlantic water further offshore, i.e., greater transport to the atmosphere. Such transport would not be expected downcurrent (north) of the bubble plumes observed by the early fall cruise reported in Westbrook et al. (2009).

Although the studies indicate these seeps do not contribute to summer atmospheric CH_4, they did not consider methane shoaling, which would allow seabed CH_4 to reach the atmosphere far downstream. Interestingly, Mau et al. (2017; Fig. 3) show data that could be interpreted as methane shoaling with elevated aqueous CH_4 forced shallower by the north-flowing SCC, rising as it crosses onshore-offshore aligned subterranean ridges. Focus area A4 shows strong increase in CH_4 from 2005-2015 (the strongest of the focus areas (**Table 1**) and in increasing *SST* over this time period, consistent with shoaling. Larger enhancement of CH_4 growth is observed north of Spitsbergen in June (**Fig. 10c**), which is the most likely location for shoaling based on detailed Svalbard bathymetry and currents (**Supp. Fig. S2**). Specifically, this is where some of the warm West Spitsbergen Current mixes with the cold, Spitsbergen Coastal Current (SCC) that would be CH_4 enriched from seabed seepage, and then flows over relatively shallow seabed towards the Hinlopen Strait. Thus, there is evidence of increasing downstream CH_4 transport to the atmosphere downcurrent of seepage off West Spitsbergen after methane shoaling, albeit not significant to overall Barents Sea emissions.

There is evidence of acceleration in the CH_4 growth nearshore off West Spitsbergen in June, but not in September (**Fig. 11**) when CH_4 growth enhancement lies in the further offshore waters that are impacted by the warm WSC. Trends in *SST* also suggest a weakening of the Percey Current in June and more so in September. Given that from June to September the SCC extends further offshore, this suggests WSC control. Similarly, the WSC eastwards leg that crosses Nordaustlandet is driving a rapid increase in *SST* in September and likely relates to the increased CH_4 trend.

The Cryosphere Discuss., https://doi.org/10.5194/tc-2018-237
Manuscript under review for journal The Cryosphere
Discussion started: 22 November 2018

4.6. Ice-Free Barents Sea

The southern Barents Sea has been ice free since at least 1850 (Walsh et al., 2016). Meanwhile the northwest Barents Sea is near ice-free year round, whereas northeast Barents Sea (around Franz Josef Land and St. Anna Trough) remains ice-covered for about half the year (**Fig. 6**). The ice coverage trends suggest most of the Barents Sea will be ice free, year-round circa 2030. This is comparable to the 2023-2036 estimate of Onarheim and Årthun (2017; Fig. 3), which also notes that the current decreasing trend lies outside the oscillation envelope since 1850. Ice records since 1850 show fairly stable sea ice through 1980 in March (within ±20%), and 1970 in September (within ±50%), decreasing to date (Walsh et al., 2016). For the Barents Sea, and other marginal Arctic seas most significant ice loss occurs in late summer (Onarheim et al., 2018).

This has implications for the Barents and Kara Seas ecosystems, and follows documented changes across the Arctic in satellite remote sensing of phytoplankton concentration (Arrigo et al., 2008; Arrigo and van Dijken, 2011; Kahru et al., 2011) and *in situ* studies (Grebmeier et al., 2006; Kędra et al., 2015). One example is a significant northwards shift (5° over 20 yrs.) of phytoplankton blooms (Neukermans et al., 2018). Ice cover changes play a key role. For example, primary productivity increases in the northern Barents and Kara Seas (**Fig. 2**) are considered caused by decreased ice cover (Slagstad et al., 2015), which has driven changes in the higher trophic levels of the pelagic and benthic community (Kędra et al., 2015).

The Barents Sea is a marginal sea between the temperate Norwegian Sea and the Arctic Basin and thus is the conduit through which lower-latitude oceanic heat is transmitted to the Arctic Basin (Onarheim and Årthun, 2017). Given the significant role the Barents Sea plays in overall Arctic ice loss - fully 25% of the loss is attributed to the Barents Sea, which comprises 4% of the Arctic Ocean including marginal seas (Smedsrud et al., 2013), implications will be significant for weather at lower latitudes, and the marine ecosystem. Seemingly counter-intuitive, sea ice reduction increases the upwards surface heat flux as ice has an insulating effect. Thus ice-loss somewhat stabilizes Arctic Basin ice, particularly during winter (Onarheim and Årthun, 2017) and may even lead to growth of ice in the Arctic Basin and northern Greenland Sea. Still, the data herein are consistent with a progressive weakening of the Percey Current, which will continue to cause ice loss off east Svalbard and warming of these waters. This agrees with Alexander et al. (2004) who concluded that the (semi-stationary due to bathymetry) Barents Sea Polar Front has shifted due to domination of Atlantic over Arctic waters.

As noted, the progression of ice loss in the south and east Barents Sea along the pathway of the Murman Coastal Current has led to a progressive loss of ice in the south Kara Sea. Thus, the balance between the two processes – heat loss to the atmosphere from and progressive transport of heat by currents to the Kara Sea are clearly shifting towards warmer. The implications of decreasing ice cover in the shallow Kara Sea are significant with respect to CH_4 emissions – the area is rich in hydrocarbon resources that currently are likely sequestered under submerged permafrost that will continue to degrade, while warming seabed temperatures will enhance microbial degradation of the vast organic material deposited over the millennia by the Ob and Yenisei Rivers. Thus, the already significant importance of Arctic CH_4 anomaly from the Kara Sea will accelerate due to feedbacks from an ice-free Barents Sea.

4.7. Future research

Oscillations with a 6-8 year timescale are suggested (e.g., **Fig. 8c**); however, the 13-year dataset is too short to investigate in detail. Extending the analysis to include more recent data (say through 2018) would span a full 2 1/2 cycles and allow investigation of correlations with other driving oceanographic atmospheric cycles, such as the NAO. This would be particularly valuable given that recent data show that the most recent two years (2016-2017) are the most extreme in terms of Barents Sea ice coverage (Oziel et al. 2016) and CH_4 anomaly (**Supp. Fig. S10; Supp. Video**). Extending the analysis forward in time clearly would provide greater insights into the complex relationship between currents and CH_4 emissions. In this regard, the long–term commitment to IASI satellite instruments (MetOp-A/IASI-A launched in 2006 and remains in service, MetOp-C/IASI-C is scheduled to launch Nov 2018) will provide invaluable long-term satellite CH_4 data.

Additionally, there is clearly need for these data to be incorporated into coupled atmospheric-oceanographic-ice models to understand in greater detail the processes underlying the changes, improving the ability to forecast trends in Arctic marine greenhouse gas emissions. Currently the strong and growing CH_4 anomaly from Novaya Zemlya and Franz Josef Land are the strongest in the Arctic, yet are not yet incorporated (or identified) in inversion models, e.g., Crevoisier et al. (2014). This identifies a key strength of satellite data, which can identify sources that are not part of an apriori (inversion model initialization of sources).

Finally, as part of this study, changes in chlorophyll were investigated with respect to changes in *SST* and CH_4. These relationships need to be evaluated in future research to tie the dramatic changes in the ecosystem and physical oceanography of the Barents and Kara Seas, leveraging the strengths of satellite data.

5. Conclusion

In this study, the global, repeat nature of satellite data was used to investigate the relationship between currents, and trends in sea surface temperature, ice extent, and methane (CH_4) anomaly for the Barents and Kara Seas for 2003-2015. Large positive CH_4 anomalies were discovered around Franz Josef Land and offshore west Novaya Zemlya in September, in areas where downstream current shoaling, with far smaller CH_4 enhancement around Svalbard, again, strongest where currents likely shoal downcurrent of seabed seepage. This highlights a major strength of satellite data: Identification of sources that are not part of an apriori used to initialize inversion models.

The strongest *SST* growth was southeast Barents Sea in June where strengthening of the warm Murman Current (an extension of the Norwegian Atlantic Current) could explain the trend, and in the south Kara Sea in September, whereas the cold southwards-flowing Percey Current weakened. These regions also exhibit the strongest CH_4 growth enhancement as well as around Franz Josef Land. Likely sources are CH_4 seepage from extensive oil and gas reservoirs underlying the central and east Barents Sea and Kara Sea; however, the spatial pattern was poorly correlated with depth and best correlated by strengthened currents that shoal.

Trends in the Barents Sea and Kara Seas will lead to an ice free Barents Sea free in about 15 years, while driving seabed warming and enhanced CH_4 emissions, particularly from areas where currents drive methane shoaling.

Acknowledgements: The research was supported by a grant from NASA ROSES2013: "A.28, The Science of TERRA AND AQUA: Long-term Satellite Data Fusion Observations of Arctic Ice Cover and Methane as a Climate Change Feedback." We thank Vladimir Ivanov, Arctic and Antarctic Research Institute, for organizing the NABOS cruise and Cathrine Lund Myrhe, Norwegian Air Research Institute (NILU), for calibration gas used during the NABOS cruise.

References

Aagaard, K. and Carmack, E. C.: The role of sea ice and other fresh water in the Arctic circulation, Journal of Geophysical Research: Oceans, 94, 14485-14498, doi: 10.1029/JC094iC10p14485, 1989.

Ackerman, S., et al.: Discriminating clear-sky from cloud with {MODIS}, Algorithm Theoretical Basis Document (MOD35), ATB-MOD-06, 129 pp., 2010.

AIRS Science Team/Joao Texeira: AIRS2RET: AIRS/Aqua L2 Standard Physical Retrieval (AIRS-only) V006. Goddard Earth Sciences Data and Information Services Center (GES DISC), Greenbelt, MD, 2016.

Alexander, M. A., et al.: The atmospheric response to realistic Arctic sea ice anomalies in an AGCM during winter, Journal of Climate, 17, 890-905, doi: 10.1175/1520-0442(2004)017<0890:Tartra>2.0.Co;2, 2004.

Alexander, M. A., et al.: Projected sea surface temperatures over the 21st century: Changes in the mean, variability and extremes for large marine ecosystem regions of Northern Oceans, Elementa Science of the Anthropocene, 6, 9, doi: 10.1525/elementa.191, 2018.

Aliabadi, A. A., et al.: Comparison of estimated atmospheric boundary layer mixing height in the Arctic and Southern Great Plains under statically stable conditions: Experimental and numerical aspects, Atmosphere-Ocean, 54, 60-74, doi: 10.1080/07055900.2015.1119100, 2016.

Archer, D., Buffett, B., and Brovkin, V.: Ocean methane hydrates as a slow tipping point in the global carbon cycle, Proceedings of the National Academy of Sciences, 106, 20596-20601, doi: 10.1073/pnas.0800885105, 2009.

Arrigo, K. R., van Dijken, G., and Pabi, S.: Impact of a shrinking Arctic ice cover on marine primary production, Geophysical Research Letters, 35, L19603, doi: 10.1029/2008GL035028, 2008.

Arrigo, K. R. and van Dijken, G. L.: Secular trends in Arctic Ocean net primary production, Journal of Geophysical Research: Oceans, 116, C09011, doi: 10.1029/2011JC007151, 2011.

Årthun, M., et al.: Quantifying the influence of Atlantic heat on Barents Sea ice variability and retreat, Journal of Climate, 25, 4736-4743, doi: 10.1175/jcli-d-11-00466.1, 2012.

Bøe, R., et al.: Sandwaves and sand transport on the Barents Sea continental slope offshore northern Norway, Marine and Petroleum Geology, 60, 34-53, doi: https://doi.org/10.1016/j.marpetgeo.2014.10.011, 2015.

Boitsov, V. D., Karsakov, A. L., and Trofimov, A. G.: Atlantic water temperature and climate in the Barents Sea, 2000–2009, ICES Journal of Marine Science, 69, 833-840, doi: 10.1093/icesjms/fss075, 2012.

Carmack, E. and McLaughlin, F.: Towards recognition of physical and geochemical change in Subarctic and Arctic Seas, Progress in Oceanography, 90, 90-104, doi: https://doi.org/10.1016/j.pocean.2011.02.007, 2011.

Chang, R. Y.-W., et al.: Methane emissions from Alaska in 2012 from CARVE airborne observations, Proceedings of the National Academy of Sciences, 111, 16694-16699, doi: 10.1073/pnas.1412953111, 2014.

Clark, R. N., Curchin, J. M., Hoefen, T. M., and Swayze, G. A.: Reflectance spectroscopy of organic compounds: 1. Alkanes, Journal of Geophysical Research, 114, E03001, doi: 10.1029/2008je003150, 2009.

Comiso, J. C.: Large decadal decline of the arctic multiyear ice cover, Journal of Climate, 25, 1176-1193, doi: 10.1175/jcli-d-11-00113.1, 2012.

Comiso, J. C., Parkinson, C. L., Gersten, R., and Stock, L.: Accelerated decline in the Arctic sea ice cover, Geophysical Research Letters, 35, L01703, doi: 10.1029/2007GL031972, 2008.

Crevoisier, C., et al.: Towards IASI-New Generation (IASI-NG): Impact of improved spectral resolution and radiometric noise on the retrieval of thermodynamic, chemistry and climate variables, Atmospheric Measurement Techniques, 7, 4367-4385, doi: 10.5194/amt-7-4367-2014, 2014.

de Boyer Montégut, C., et al.: Mixed layer depth over the global ocean: An examination of profile data and a profile-based climatology, Journal of Geophysical Research: Oceans, 109, doi: 10.1029/2004JC002378, 2004.

Desjardins, R. L., et al.: The challenge of reconciling bottom-up agricultural methane emissions inventories with top-down measurements, Agricultural and Forest Meteorology, 248, 48-59, doi: 10.1016/j.agrformet.2017.09.003, 2018.

Dlugokencky, E. J., Nisbet, E. G., Fisher, R., and Lowry, D.: Global atmospheric methane: Budget, changes and dangers, Philosophical Transactions of the Royal Society A: Mathematical, Physical and Engineering Sciences, 369, 2058-2072, doi: 10.1098/rsta.2010.0341, 2011.

The Cryosphere Discuss., https://doi.org/10.5194/tc-2018-237
Manuscript under review for journal The Cryosphere
Discussion started: 22 November 2018

Fetterer, F., et al.: Sea Ice Index (version 3). National Snow and Ice Data Center (NSDIC), Boulder, CO, 2017.

Frankignoul, C.: Sea surface temperature anomalies, planetary waves, and air-sea feedback in the middle latitudes, 23, 357-390, doi: 10.1029/RG023i004p00357, 1985.

Gammelsrød, T., et al.: Mass and heat transports in the NE Barents Sea: Observations and models, Journal of Marine Systems, 75, 56-69, doi: 10.1016/j.jmarsys.2008.07.010, 2009.

Gawarkiewicz, G. and Plueddemann, A. J.: Topographic control of thermohaline frontal structure in the Barents Sea Polar Front on the south flank of Spitsbergen Bank, Journal of Geophysical Research: Oceans, 100, 4509-4524, doi: 10.1029/94JC02427, 1995.

Ghosh, A., et al.: Variations in global methane sources and sinks during 1910–2010, Atmospheric Chemistry and Physics, 15, 2595-2612, doi: 10.5194/acp-15-2595-2015, 2015.

Graversen, R. G., et al.: Vertical structure of recent Arctic warming, Nature, 451, 53-56, doi: 10.1038/nature06502, 2008.

Grebmeier, J. M., et al.: A Major Ecosystem Shift in the Northern Bering Sea, Science, 311, 1461-1464, doi: 10.1126/science.1121365, 2006.

Gruber, N., et al.: The vulnerability of the carbon cycle in the 21st century: An assessment of carbon-climate-human interactions. In: The Global Carbon Cycle, Field, C. B. and Raupach, M. R. (Eds.), Island Press, Washington D.C., 2004.

Harris, C. L., Plueddemann, A. J., and Gawarkiewicz, G. G.: Water mass distribution and polar front structure in the western Barents Sea, Journal of Geophysical Research: Oceans, 103, 2905-2917, doi: 10.1029/97JC02790, 1998.

Hoegh-Guldberg, O. and Bruno, J. F.: The impact of climate change on the world's marine ecosystems, Science, 328, 1523-1528, doi: 10.1126/science.1189930, 2010.

Höglund-Isaksson, L.: Bottom-up simulations of methane and ethane emissions from global oil and gas systems 1980 to 2012, Environmental Research Letters, 12, 024007, doi: 10.1088/1748-9326/aa583e, 2017.

IPCC: Climate Change 2007: Synthesis Report. Contribution of Working Groups I, II, and III to the Fourth Assessment Report of the Intergovernmental Panel on Climate Change, IPCC, Geneva, Switzerland, 104 pp., 2007.

IPCC: Working Group 1 Contribution to the IPCC Fifth Assessment Report Climate Change 2013-The Physical Science Basis, International Panel on Climate Change, IPCC Secretariat, Geneva, Switzerland, 2216 pp., 2013.

Jakobsson, M., et al.: The International Bathymetric Chart of the Arctic Ocean (IBCAO) Version 3.0, Geophysical Research Letters, 39, L12609, doi: 10.1029/2012GL052219, 2012.

James, R. H., et al.: Effects of climate change on methane emissions from seafloor sediments in the Arctic Ocean: A review, Limnology and Oceanography, 61, 5281-5299, doi: 10.1002/lno.10307, 2016.

John, J. G., et al.: Climate versus emission drivers of methane lifetime against loss by tropospheric OH from 1860–2100, Atmospheric Chemistry and Physics, 12, 12021-12036, doi: 10.5194/acp-12-12021-2012, 2012.

Juahir, H., et al.: Hydrological trend analysis due to land use changes at Langat River Basin, Environment Asia, 3, 20-31, doi, http://hdl.handle.net/10535/7032, 2010.

Judd, A. and Hovland, M.: Seabed fluid flow: The impact on geology, biology and the marine environment, Cambridge University Press, Cambridge, UK, pp. 492, 2007.

Kahru, M., Brotas, V., Manzano-Sarabia, M., and Mitchell, B. G.: Are phytoplankton blooms occurring earlier in the Arctic?, Global Change Biology, 17, 1733-1739, doi: 10.1111/j.1365-2486.2010.02312.x, 2011.

Kędra, M., et al.: Status and trends in the structure of Arctic benthic food webs, Polar Research, 34, 23775, doi: 10.3402/polar.v34.23775, 2015.

Kolstad, E. W.: A QuikSCAT climatology of ocean surface winds in the Nordic seas: Identification of features and comparison with the NCEP/NCAR reanalysis, Journal of Geophysical Research: Atmospheres, 113, D11106, doi: 10.1029/2007JD008918, 2008.

Kort, E. A., Frankenberg, C., Miller, C. E., and Oda, T.: Space-based observations of megacity carbon dioxide, Geophysical Research Letters, 39, L17806, doi: 10.1029/2012GL052738, 2012.

Koyama, T., Stroeve, J., Cassano, J., and Crawford, A.: Sea ice loss and Arctic cyclone activity from 1979 to 2014, Journal of Climate, 30, 4735-4754, doi: 10.1175/jcli-d-16-0542.1, 2017.

Kubryakov, A., Stanichny, S., and Zatsepin, A.: River plume dynamics in the Kara Sea from altimetry-based Lagrangian model, satellite salinity and chlorophyll data, Remote Sensing of Environment, 176, 177-187, doi: 10.1016/j.rse.2016.01.020, 2016.

Lammers, S., Suess, E., and Hovland, M.: A large methane plume east of Bear Island (Barents Sea): implications for the marine methane cycle, Geologisher Rundschau, 84, 59-66, doi: 10.1007/bf00192242, 1995.

Lee, S., et al.: Revisiting the cause of the 1989–2009 Arctic surface warming using the surface energy budget: Downward infrared radiation dominates the surface fluxes, Geophysical Research Letters, 44, 10,654-610,661, doi: 10.1002/2017GL075375, 2017.

Leifer, I.: Characteristics and scaling of bubble plumes from marine hydrocarbon seepage in the Coal Oil Point seep field, Journal Geophysical Research, 115, C11014, doi: 10.1029/2009JC005844, 2010.

Leifer, I., Chernykh, D., Shakhova, N., and Semiletov, I.: Sonar gas flux estimation by bubble insonification: Application to methane bubble flux from seep areas in the outer Laptev Sea, The Cryosphere, 11, 1333-1350, doi: 10.5194/tc-11-1333-2017, 2017.

Leifer, I., Jeuthe, H., Gjøsund, S. H., and Johansen, V.: Engineered and natural marine seep, bubble-driven buoyancy flows, Journal of Physical Oceanography, 39, 3071-3090, doi: 10.1175/2009JPO4135.1, 2009.

Leifer, I. and MacDonald, I. R.: Dynamics of the gas flux from shallow gas hydrate deposits: Interaction between oily hydrate bubbles and the oceanic environment, Earth and Planetary Science Letters, 210, 411-424, doi: 10.1016/S0012-821X(03)00173-0, 2003.

Leifer, I. and Patro, R.: The bubble mechanism for methane transport from the shallow seabed to the surface: A review and sensitivity study, Continental Shelf Research, 22, 2409-2428, doi: 10.1016/S0278-4343(02)00065-1, 2002.

Leifer, I., et al.: The fate of bubbles in a large, intense bubble plume for stratified and unstratified water: Numerical simulations of 22/4b expedition field data, Journal of Marine and Petroleum Geology, 68B, 806-823, doi: 10.1016/j.marpetgeo.2015.07.025, 2015.

Leifer, I., et al.: Remote sensing atmospheric trace gases with infrared imaging spectroscopy, EOS, Transactions of the AGU, 93, 525, doi: 10.1029/2012EO500006, 2012.

Li, S. and McClimans, T. A.: The effects of winds over a barotropic retrograde slope current, Continental Shelf Research, 18, 457-485, doi: 10.1016/S0278-4343(97)00077-0, 1998.

Liang, Q., et al.: Deriving global OH abundance and atmospheric lifetimes for long-lived gases: A search for CH3CCl3 alternatives, Journal of Geophysical Research: Atmospheres, 122, 11,914-911,933, doi: 10.1002/2017JD026926, 2017.

Lien, V. S., Schlichtholz, P., Skagseth, Ø., and Vikebø, F. B.: Wind-driven Atlantic water flow as a direct mode for reduced Barents Sea ice cover, Journal of Climate, 30, 803-812, doi: 10.1175/jcli-d-16-0025.1, 2017.

Lien, V. S., Vikebø, F. B., and Skagseth, Ø.: One mechanism contributing to co-variability of the Atlantic inflow branches to the Arctic, Nature Communications, 4, 1488, doi: 10.1038/ncomms2505, 2013.

Loeng, H.: Features of the physical oceanographic conditions of the Barents Sea, Polar Research, 10, 5-18, doi: 10.1111/j.1751-8369.1991.tb00630.x, 1991.

Loeng, H., Ozhigin, V., and Ådlandsvik, B.: Water fluxes through the Barents Sea, ICES Journal of Marine Science, 54, 310-317, doi: 10.1006/jmsc.1996.0165, 1997.

MacDonald, I.: Remote sensing and sea-truth measurements of methane flux to the atmosphere (HYFLUX project), US Department of Energy, National Energy Technology Laboratory,, 164 pp., 2011.

MacDonald, I. R., et al.: HYFLUX: Remote sensing and sea truth of CH_4 flux from the Gulf of Mexico seep system, Lake Baikal, Russia, 6-12 Sept. 2010 2010.

Manabe, S. and Stouffer, R. J.: Sensitivity of a global climate model to an increase of CO2 concentration in the atmosphere, Journal of Geophysical Research: Oceans, 85, 5529-5554, doi: 10.1029/JC085iC10p05529, 1980.

Maslowski, W., et al.: On climatological mass, heat, and salt transports through the Barents Sea and Fram Strait from a pan-Arctic coupled ice-ocean model simulation, Journal of Geophysical Research: Oceans, 109, doi: 10.1029/2001JC001039, 2004.

Mau, S., et al.: Widespread methane seepage along the continental margin off Svalbard - from Bjørnøya to Kongsfjorden, Scientific Reports, 7, 42997, doi: 10.1038/srep42997, 2017.

McClimans, T. A.: Entrainment/detrainment along river plumes. In: Recent Research Advances in the Fluid Mechanics of Tturbulent Jets and Plumes, Davies, P. A. and Valente Neves, M. J. (Eds.), Kluwer Academic Publishers, Dordrecht, Germany, 1994.

McClimans, T. A., Johannesseen, B. O., and Nilsen, J. H.: Laboratory simulation of fronts between the various water masses in the Kara Sea, Pushkin, St. Petersburg, Russia1999, 338-348.

McClimans, T. A., et al.: Transport processes in the Kara Sea, Journal of Geophysical Research: Oceans, 105, 14121-14139, doi: 10.1029/1999JC000012, 2000.

McClimans, T. A. and Nilsen, J. H.: Laboratory simulation of the ocean currents in the Barents sea, Dynamics of Atmospheres and Oceans, 19, 3-25, doi: 10.1016/0377-0265(93)90030-B, 1993.

Moore, G. W. K.: The Novaya Zemlya Bora and its impact on Barents Sea air-sea interaction, Geophysical Research Letters, 40, 3462-3467, doi: 10.1002/grl.50641, 2013.

Myhre, C. L., et al.: Extensive release of methane from Arctic seabed west of Svalbard during summer 2014 does not influence the atmosphere, Geophysical Research Letters, 43, 2016GL068999, doi: 10.1002/2016GL068999, 2016.

NASA: Ocean Biology DAAC (OB.DAAC). 2015.

Nauw, J., Linke, P., and Leifer, I.: Bubble momentum plume as a possible mechanism for an early breakdown of the seasonal stratification in the northern North Sea, Journal of Marine and Petroleum Geology, 68, 789-805, doi: 10.1016/j.marpetgeo.2015.05.003, 2015.

Neukermans, G., Oziel, L., and Babin, M.: Increased intrusion of warming Atlantic water leads to rapid expansion of temperate phytoplankton in the Arctic, Global Change Biology, In Press, doi: 10.1111/gcb.14075, 2018.

Nisbet, E. G., Dlugokencky, E. J., and Bousquet, P.: Methane on the rise—Again, Science, 343, 493-495, doi: 10.1126/science.1247828, 2014.

NRC: The Arctic in the Anthropocene: Emerging Research Questions, The National Academies Press, Washington, DC,, pp. 224, 2014.

Onarheim, I. H. and Årthun, M.: Toward an ice-free Barents Sea, Geophysical Research Letters, 44, 8387-8395, doi: 10.1002/ 2017GL074304, 2017.

Onarheim, I. H., Eldevik, T., Smedsrud, L. H., and Stroeve, J. C.: Seasonal and regional manifestation of Arctic Sea ice loss, Journal of Climate, 31, 4917-4932, doi: 10.1175/jcli-d-17-0427.1, 2018.

Önöz, B. and Bayazit, M.: The power of statistical tests for trend detection, Turkish Journal of Engineering and Environmental Sciences, 27, 247-251, doi, 2003.

Osterkamp, T. E.: Subsea Permafrost. In: Climate and Oceans, Steele, J. H., Thorpe, S. A., and Turekian, K. K. (Eds.), Academic Press, London UK, 2010.

Overland, J. E. and Wang, M.: When will the summer Arctic be nearly sea ice free?, Geophysical Research Letters, 40, 2097-2101, doi: 10.1002/grl.50316, 2013.

Ozhigin, V. K., et al.: The Barents Sea. In: The Barents Sea - ecosystem, resources, management. Half a century of Russian - Norwegian cooperation, Jakobsen, T. and Ozhigin, V. K. (Eds.), Tapir Academic Press, Trondheim, Norway, 2011.

Oziel, L., Sirven, J., and Gascard, J. C.: The Barents Sea frontal zones and water masses variability (1980–2011), Ocean Science, 12, 169-184, doi: 10.5194/os-12-169-2016, 2016.

Piechura, J. and Walczowski, W.: Warming of the West Spitsbergen current and sea ice North of Svalbard, Oceanologia, 51, 147-164, doi, http://agro.icm.edu.pl/agro/element/bwmeta1.element.agro-article-fc388afa-b7bf-4387-8f5b-6285707fed8e, 2009.

Polyak, L., et al.: Benthic foraminiferal assemblages from the Southern Kara Sea - A river-influenced Arctic marine environment, The Journal of Foraminiferal Research, 32, 252-273, doi: 10.2113/32.3.252, 2002.

Prather, M. J., Holmes, C. D., and Hsu, J.: Reactive greenhouse gas scenarios: Systematic exploration of uncertainties and the role of atmospheric chemistry, Geophysical Research Letters, 39, L09803, doi: 10.1029/2012GL051440, 2012.

Reeburgh, W. S.: Global methane biogeochemistry. In: The Atmosphere. Treatise on Geochemistry, Keeling, R. (Ed.), Elsevier-Pergamon, Oxford, 2003.

Reeburgh, W. S.: Oceanic methane biogeochemistry, Chemical Reviews, 107, 486-513, doi: 10.1021/cr050362v, 2007.

Rehder, G., Keir, R. S., Suess, E., and Rhein, M.: Methane in the Northern Atlantic controlled by microbial oxidation and atmospheric history, Geophysical Research Letters, 26, 587-590, doi: 10.1029/1999GL900049, 1999.

Rehder, G., et al.: Controls on methane bubble dissolution inside and outside the hydrate stability field from open ocean field experiments and numerical modeling, Marine Chemistry, 114, 19-30, doi: 10.1016/j.marchem.2009.03.004, 2009.

Rekacewicz, P.: https://www.grida.no/resources/7482) last access: January 2018 2018.

Rise, L., Bellec, V. K., Chand, S., and Bøe, R.: Pockmarks in the southwestern Barents Sea and Finnmark fjords, Norwegian Journal of Geology, 94, 263-282, doi: 10.17850/njg94-4-02, 2015.

Saunois, M., et al.: The global methane budget: 2000-2012, Earth System Science Data Discussion, 2016, 1-79, doi: 10.5194/essd-2016-25, 2016.

Schweiger, A. J., Lindsay, R. W., Vavrus, S., and Francis, J. A.: Relationships between Arctic Sea ice and clouds during autumn, Journal of Climate, 21, 4799-4810, doi: 10.1175/2008jcli2156.1, 2008.

Screen, J. A. and Simmonds, I.: The central role of diminishing sea ice in recent Arctic temperature amplification, Nature, 464, 1334-1337, doi: 10.1038/nature09051, 2010.

SEADAS: https://seadas.gsfc.nasa.gov/help/, last access: Jan 1 2016, https://seadas.gsfc.nasa.gov/help/, 2017.

Sen, P. K.: Estimates of the regression coefficient based on Kendall's tau, Journal of the American Statistical Association, 63, 1379-1389, doi: 10.2307/2285891, 1968.

Shakhova, N., et al.: Current rates and mechanisms of subsea permafrost degradation in the East Siberian Arctic Shelf, Nature Communications, 8, 15872, doi: 10.1038/ncomms15872, 2017.

Shakhova, N., et al.: Ebullition and storm-induced methane release from the East Siberian Arctic Shelf, Nature Geoscience, 7, 64-70, doi: 10.1038/ngeo2007, 2013.

Shakhova, N., et al.: The East Siberian Arctic Shelf: Towards further assessment of permafrost-related methane fluxes and role of sea ice, Philosophical Transactions of the Royal Society A: Mathematical, Physical and Engineering Sciences, 373, 1-13, doi: 10.1098/rsta.2014.0451, 2015.

Skagseth, Ø., et al.: Volume and heat transports to the Arctic Ocean via the Norwegian and Barents Seas. In: Arctic–Subarctic Ocean Fluxes: Defining the Role of the Northern Seas in Climate, Dickson, R. R., Meincke, J., and Rhines, P. (Eds.), Springer Netherlands, Dordrecht, 2008.

Slagstad, D., Wassmann, P. F. J., and Ellingsen, I.: Physical constrains and productivity in the future Arctic Ocean, Frontiers in Marine Science, 2, doi: 10.3389/fmars.2015.00085, 2015.

Smedsrud, L. H., et al.: The role of the Barents Sea in the Arctic climate system, Reviews of Geophysics, 51, 415-449, doi: 10.1002/rog.20017, 2013.

Sokolov, S. Y., et al.: Mapping of sound scattering objects in the northern part of the Barents Sea and their geological interpretation, Oceanology, 57, 593-599, doi: 10.1134/s000143701704018x, 2017.

Solheim, A. and ElverhøI, A.: A pockmark field in the Central Barents Sea; gas from a petrogenic source?, Polar Research, 3, 11-19, doi: 10.1111/j.1751-8369.1985.tb00492.x, 1985.

Solomon, E., Kastner, M., MacDonald, I. R., and Leifer, I.: Considerable methane fluxes to the atmosphere from hydrocarbon seeps in the Gulf of Mexico, Nature Geoscience, 2, 561-565, doi: 10.1038/NGEO574, 2009.

Stedmon, C. A., Amon, R. M. W., Rinehart, A. J., and Walker, S.: The supply and characteristics of Colored Dissolved Organic Matter (CDOM) in the Arctic Ocean: Pan Arctic trends and differences, Marine Chemistry, 124, 108-118, doi: 10.1016/j.marchem.2010.12.007, 2011.

Stiansen, J. E., et al.: Joint PINRO/IMR report on the state of the Barents Sea ecosystem 2005/2006, 2006. 122, doi, 2006.

Stiansen, J. E., et al.: Joint Norwegian-Russian environmental status 2008. Report on the Barents Sea Ecosystem. Part II – Complete report, Norwegian Marine Data Center (NMDC)1502-8828, 375 pp., 2009.

Stroeve, J. C., et al.: Changes in Arctic melt season and implications for sea ice loss, Geophysical Research Letters, 41, 1216-1225, doi: 10.1002/2013GL058951, 2014.

Svendsen, H., et al.: The physical environment of Kongsfjorden–Krossfjorden, an Arctic fjord system in Svalbard, Polar Research, 21, 133-166, doi: 10.1111/j.1751-8369.2002.tb00072.x, 2002.

Tarnocai, C., et al.: Soil organic carbon pools in the northern circumpolar permafrost region, Global Biogeochemical Cycles, 23, GB2023, doi: 10.1029/2008gb003327, 2009.

Thonat, T., et al.: Detectability of Arctic methane sources at six sites performing continuous atmospheric measurements, Atmospheric Chemistray and Physics, 17, 8371-8394, doi: 10.5194/acp-17-8371-2017, 2017.

Tratt, D. M., et al.: Airborne visualization and quantification of discrete methane sources in the environment, Remote Sensing of Environment, 154, 74-88, doi: 10.1016/j.rse.2014.08.011, 2014.

Turner, A. J., et al.: A large increase in U.S. methane emissions over the past decade inferred from satellite data and surface observations, Geophysical Research Letters, 43, 2218-2224, doi: 10.1002/2016GL067987, 2016.

Vinje, T. and Kvambekk, Å. S.: Barents Sea drift ice characteristics, Polar Research, 10, 59-68, doi: 10.3402/polar.v10i1.6728, 1991.

Walsh, J. E., Fetterer, F., Scott Stewart, J., and Chapman, W. L.: A database for depicting Arctic sea ice variations back to 1850, Geographical Review, 107, 89-107, doi: 10.1111/j.1931-0846.2016.12195.x, 2016.

The Cryosphere Discuss., https://doi.org/10.5194/tc-2018-237
Manuscript under review for journal The Cryosphere
Discussion started: 22 November 2018

The Cryosphere Discussions

Warzinski, R. P., et al.: Dynamic morphology of gas hydrate on a methane bubble in water: Observations and new insights for hydrate film models, Geophysical Research Letters, 41, 6841-6847, doi: 10.1002/2014GL061665, 2014.

Westbrook, G. K., et al.: Estimation of gas hydrate concentration from multi-component seismic data at sites on the continental margins of NW Svalbard and the Storegga region of Norway, Marine and Petroleum Geology, 25, 744-758, doi: 10.1016/j.marpetgeo.2008.02.003, 2008.

Westbrook, G. K., et al.: Escape of methane gas from the seabed along the West Spitsbergen continental margin, Geophysical Research Letters, 36, doi: 10.1029/2009gl039191, 2009.

Whitehead, J. A. and Salzig, J.: Rotating channel flow: Control and upstream currents, Geophysical & Astrophysical Fluid Dynamics, 95, 185-226, doi: 10.1080/03091920108203725, 2001.

Wofsy, S. C.: HIAPER Pole-to-Pole Observations (HIPPO): fine-grained, global-scale measurements of climatically important atmospheric gases and aerosols, Philosophical Transactions of the Royal Society A: Mathematical, Physical and Engineering Sciences, 369, 2073-2086, doi: 10.1098/rsta.2010.0313, 2011.

Xiong, X., et al.: Mid-upper tropospheric methane retrieval from IASI and its validation, Atmospheric Measurement Techniques, 6, 2255-2265, doi: 10.5194/amt-6-2255-2013, 2013.

Xiong, X., Han, Y., Liu, Q., and Weng, F.: Comparison of atmospheric methane retrievals trom AIRS and IASI, IEEE Journal of Selected Topics in Applied Earth Observations and Remote Sensing, 9, 3297-3303, doi: 10.1109/JSTARS.2016.2588279, 2016.

Yamamoto-Kawai, M., et al.: Freshwater budget of the Canada Basin, Arctic Ocean, from salinity, δ 18O, and nutrients, Journal of Geophysical Research: Oceans, 113, C01007, doi: 10.1029/2006JC003858, 2008.

Yurganov, L. and Leifer, I.: Estimates of methane emission rates from some Arctic and sub-Arctic areas based on orbital interferometer IASI data, Current Problems in Remote Sensing of Earth from Space (Sovremennye Problemy Distantsionnogo Zondirovaniya Zemli iz Kosmosa), 13, 173-183, doi: 10.21046/2070-7401-2016-13-2-107-119, 2016a.

Yurganov, L., Leifer, I., and Lund-Myhre, C.: Seasonal and interannual variability of atmospheric methane over Arctic Ocean from satellite data, Current Problems in Remote Sensing of Earth from Space (Sovremennye Problemy Distantsionnogo Zondirovaniya Zemli iz Kosmosa), 13, 107-119, doi: 10.21046/2070-7401-2016-13-2-107-119, 2016.

Yurganov, L. N. and Leifer, I.: Abnormal concentrations of atmospherc methane over the Sea of Okhotsk during 2015/2016 winter, Current Problems in Remote Sensing of Earth from Space (Sovremennye problemy distantsionnogo zondirovaniya zemli iz kosmosa), 1, 231-234, doi: 10.21046/2070-7401-2016-13-3-231-234, 2016b.

Yurganov, L., Leifer, I., and Lund-Myhre, C.: Seasonal and interannual variability of atmospheric methane over Arctic Ocean from satellite data, Current Problems in Remote Sensing of Earth from Space (Sovremennye Problemy Distantsionnogo Zondirovaniya Zemli iz Kosmosa), 13, 107-119, doi: 10.21046/2070-7401-2016-13-2-107-119, 2016.

The Cryosphere Discuss., https://doi.org/10.5194/tc-2018-237
Manuscript under review for journal The Cryosphere
Discussion started: 22 November 2018

TABLES

Table 1. Slopes of *SST* (°C yr^{-1}), CH_4 (ppb yr^{-1}), and CH_4' (ppb yr^{-1}) for focus boxes. [a]

Box	*SST*	CH_4	CH_4	CH_4' (Barents)[b]	CH_4' (Arctic)[c]
	2003-2015	2003-2015	2005-2015	2003-2015	2003-2015
A1	0.102	3.35	3.26	0.179	0.0750
A2	0.0319	3.49	3.38	0.267	0.213
A3	0.00178	3.19	3.17	-0.0185	0.00574
A4	0.0867	3.37	3.60	0.310	0.391
A5	0.0279	3.10	3.22	0.0105	0.0319
A6	0.00259	3.07	3.24	-0.0123	0.0548
A7	0.0323	3.06	3.27	-0.0460	-0.119
A8	0.0552	3.11	3.35	0.0642	-0.0544
A9	0.145	3.20	3.44	0.103	0.109
A10	0.0527	3.32	3.51	0.122	0.0613

[a] *SST* – Sea Surface Temperature, CH_4' – methane anomaly.
[b] CH_4' relative to the Barents Sea
[c] CH_4' relative to the Arctic Ocean

The Cryosphere Discuss., https://doi.org/10.5194/tc-2018-237
Manuscript under review for journal The Cryosphere
Discussion started: 22 November 2018

FIGURE CAPTIONS

Figure 1 a) Arctic and sub-arctic methane (CH_4), 0.5° gridded, 0-4 km altitude, 2016, from the Infrared Atmospheric Sounding Interferometer (IASI); mountainous regions blanked. Data were filtered as in Yurganov and Leifer (2016a). Data key on panel.

Figure 2 a) Map of the Arctic Basin, showing study area (Blue Square) and average January and September 2003-2015 ice extent. **b)** Bathymetry of the study area (87.468 N, 1.219E; 72.056N, 0.173E; 63.008N, 48.05E; 69.707N, 82.793E) from Jakobsson et al. (2012). Dashed black line shows approximate Barents Sea boundaries. Dashed white line shows edge of submerged permafrost from Osterkamp (2010). Star shows scoping study pixels location.

Figure 3. Comparison of the sea surface temperature (*SST)* and methane (CH_4) for 2003-2015 for pixels between Franz Josef Land and Novaya Zemlya (**Fig. 2b, Star, Supp. Table 1, Box A2**). Red diamonds show *SST* and CH_4 averages within the study area. Blue and green ovals highlight pixels with different CH_4 trends for *SST* (all CH_4), and (CH_4>1925 ppb), respectively.

Figure 4. a) Currents for Barents and nearby seas, bathymetry features, and focus-area locations. Green, red, and blue arrows are coastal, warm Atlantic origin, and cold polar currents, respectively. Broken lines illustrate current subduction. Bathymetry from Jakobsson et al. (2012). **b)** Monthly ice extent for 2015. Focus study boxes (numbered); coordinates listed in **Supp. Table S1**. Barents Sea currents adapted from Stiansen et al. (2006); see **Supp. Fig. S2** for greater detail for Svalbard area; for Kara Sea area from Polyak et al. (2002); see **Supp. Fig. S2** for greater detail. For Barents Sea Opening area from Bøe et al. (2015).

Figure 5. a) Surface *in situ* methane (CH_4) during northward Barents Sea transect on the *R/V Akademik Federov* for 21 Aug. 2013. Also shown is the 300-m depth contour and edges of the Murman Coastal Current, from PINRO (http://www.pinro.ru/labs/hid/kolsec1_e.htm). Data key on figure. **b)** CH_4 profiles during northerly and southerly transits, labeled.

Figure 6. Ice-free months from 2003 to 2015 for focus boxes for **a)** Northern Barents (A1-A3), **b)** Northwest of Barents (A4-A6), and **c)** Southern Barents (A7-A10). Box names on panels. See **Fig. 4a** and **Supp. Table S1** for locations.

Figure 7. Sea surface temperature (*SST*) time series for 2003 to 2015 for focus box areas **a)** Northern Barents (A1-A3), **b)** Northwest of Barents (A4-A6), and **c)** Southern Barents (A7-A10). Annual values are average of all months, generally May-October, which are ice-free. Box names on panel a. Data key on figure.

Figure 8. Focus study area methane (CH_4) for 2003 to 2015 for **a)** Northern Barents study boxes, **b)** Northwest of Barents study boxes, and **c)** Barents Sea focus study boxes. Annual data and 3 year, rolling-average data shown. Anomaly is relative to entire Barents Sea. Data key on figure.

Figure 9. Mean values for 2003 to 2015 of sea surface temperature (*SST*) for **a**) June and **b**) September. Mean methane (CH_4) concentration for **c**) June and **d**) September. Median ice edge for same period is shown. Years with reduced ice extent contribute to values of *SST* north of this ice edge. Data key on figure.

Figure 10. Linear trends for 2003 to 2015 of sea surface temperature (*dSST/dt*) for **a**) June and **b**) September. Methane concentration trend (dCH_4/dt) for **c**) June and **d**) September. ND – not detectable – failed statistical test. Blue, black dashed lines shows 100 and 50 m contour, respectively. Data key on figure.

1241 FIGURES

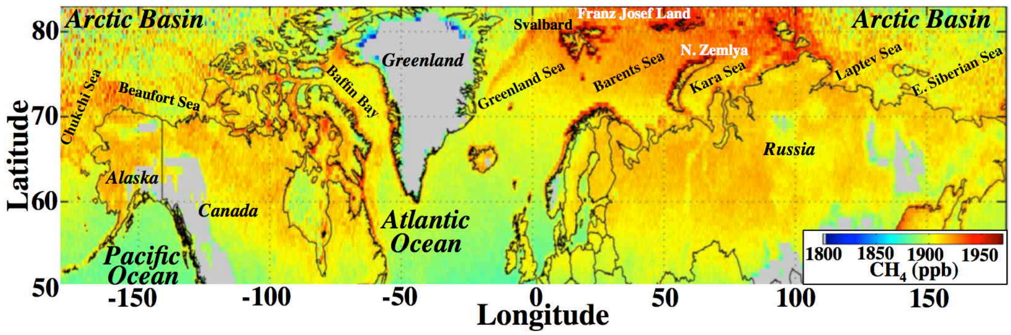

1242

1243 **Figure 1** Arctic and sub-arctic methane (CH_4), 0.5° gridded, 0-4 km altitude, 2016, from Infrared
1244 Atmospheric Sounding Interferometer (IASI); mountainous regions blanked. Data were filtered as in
1245 Yurganov and Leifer (2016a). Data key on panel. For polar stereographic view see **Supp. Fig. S8** and
1246 Supplemental Movie showing entire time series.

The Cryosphere Discuss., https://doi.org/10.5194/tc-2018-237
Manuscript under review for journal The Cryosphere
Discussion started: 22 November 2018

The Cryosphere Discussions
Open Access

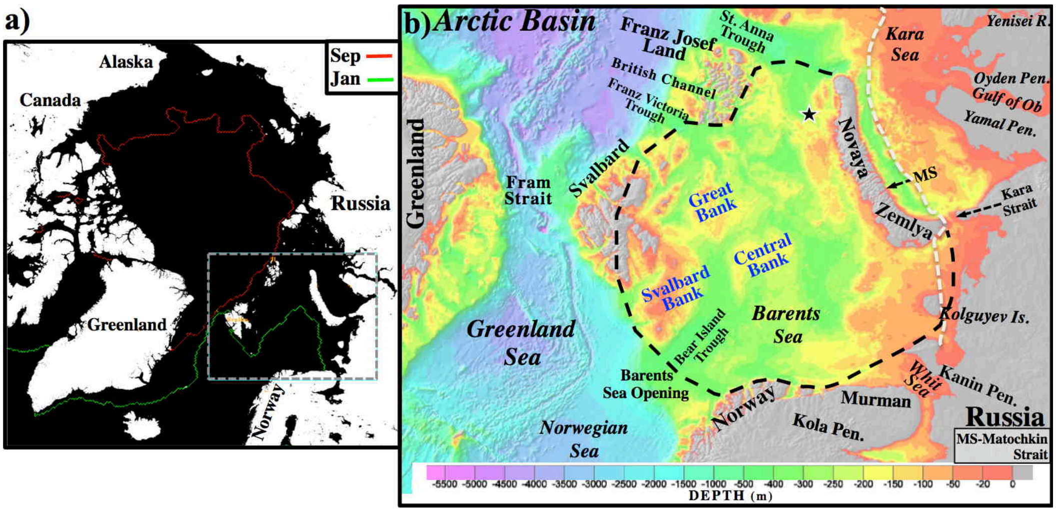

1247
1248 **Figure 2 a)** Arctic map, showing study area (Blue Square) and average January and September 2003-
1249 2015 ice extent. **b)** Bathymetry of the study area (87.468 N, 1.219E; 72.056N, 0.173E; 63.008N, 48.05E;
1250 69.707N, 82.793E) from Jakobsson et al. (2012). Dashed black line shows approximate Barents Sea
1251 boundaries. Dashed white line shows edge of submerged permafrost from Osterkamp (2010). Star shows
1252 scoping study pixels location. Depth data key on panel.

The Cryosphere Discuss., https://doi.org/10.5194/tc-2018-237
Manuscript under review for journal The Cryosphere
Discussion started: 22 November 2018

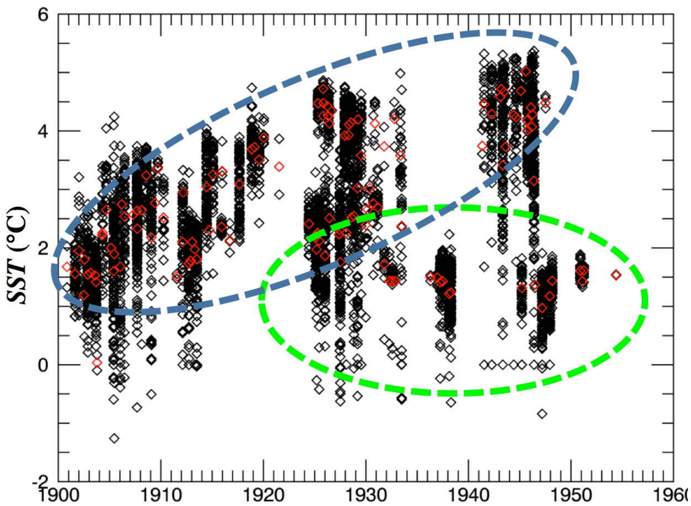

1253
1254 **Figure 3**. Comparison of the sea surface temperature (*SST)* and methane (CH_4) for 2003-2015 for pixels
1255 between Franz Josef Land and Novaya Zemlya (**Fig. 2b, Star, Supp. Table 1, Box A2**). Red diamonds
1256 show monthly *SST* and CH_4 averages within the study area. Blue and green ovals highlight pixels with
1257 different CH_4 trends for *SST* (all CH_4), and (CH_4>1925 ppb), respectively.

The Cryosphere Discuss., https://doi.org/10.5194/tc-2018-237
Manuscript under review for journal The Cryosphere
Discussion started: 22 November 2018

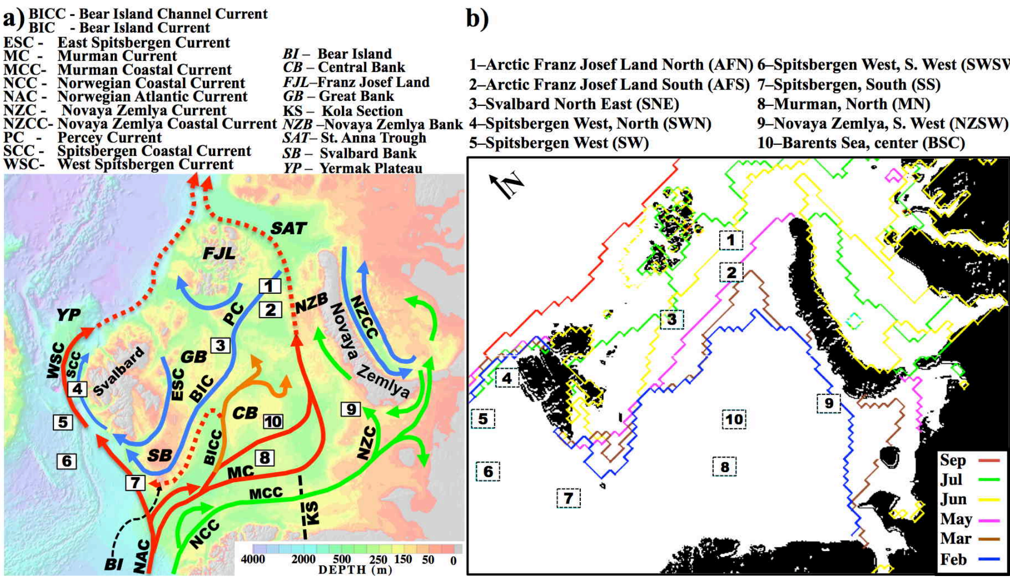

Figure 4. a) Simplified currents for Barents and nearby seas, bathymetry features, and focus-area boxes. Green, red, and blue arrows are coastal, warm Atlantic origin, and cold polar currents, respectively. Broken lines illustrate current subduction. Bathymetry from Jakobsson et al. (2012). **b)** Monthly ice extent for 2015. Focus study boxes (numbered); coordinates listed in **Supp. Table S1**. Arrow points to North Pole. Barents Sea currents adapted from Stiansen et al. (2006); for near Svalbard from Loeng (1991); see **Supp. Fig. S2** for greater detail for Svalbard area; for Kara Sea area from Polyak et al. (2002); see **Supp. Fig. S1** for greater detail. For Barents Sea Opening area from Bøe et al. (2015). East Barents Sea Currents from Ozhigin et al. (2011)

The Cryosphere Discuss., https://doi.org/10.5194/tc-2018-237
Manuscript under review for journal The Cryosphere
Discussion started: 22 November 2018

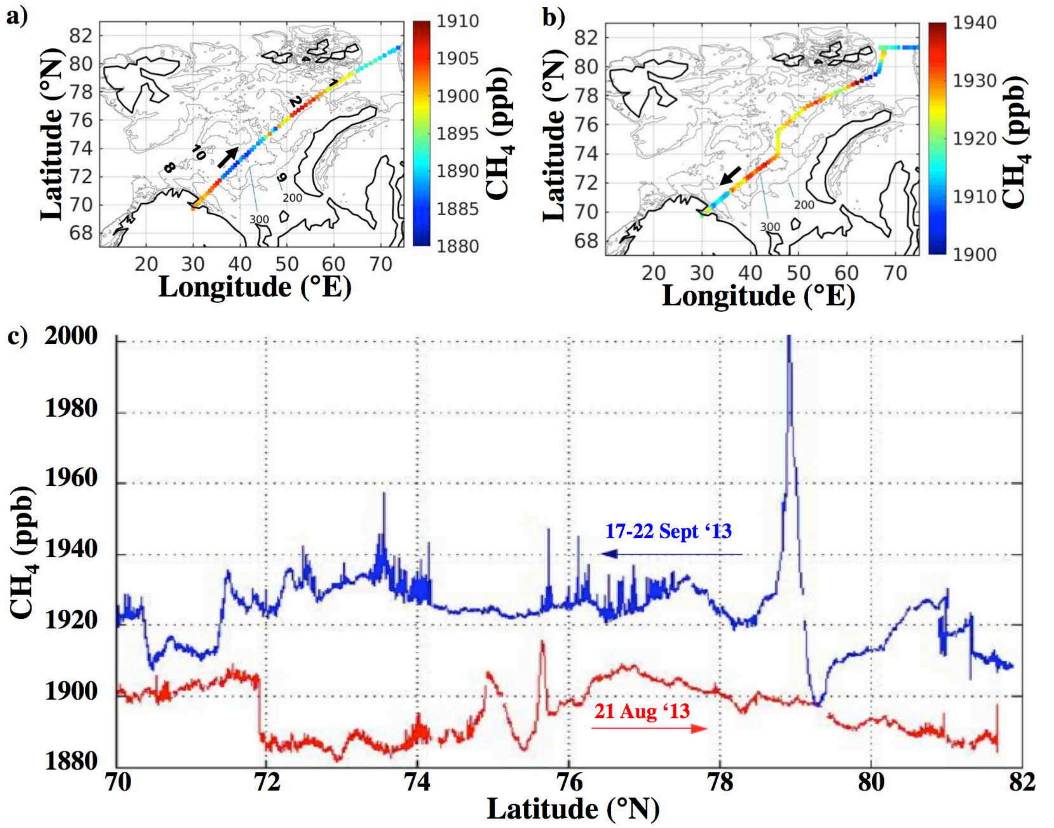

1267
1268 **Figure 5.** Surface *in situ* methane (CH_4) on the *R/V Akademik Fyodorov* for Barents Sea **a)** northwards
1269 transect for 21 Aug. 2013. Focus areas along pathway shown. **b)** Southwards transect for 17-22 Sept.
1270 2013. Also shown is the 300-m depth contour and edges of the Murman Coastal Current, from PINRO
1271 (http://www.pinro.ru/labs/hid/kolsec1_e.htm). Data key on figure. **c)** CH_4 profiles during northerly and
1272 southerly transits, labeled.

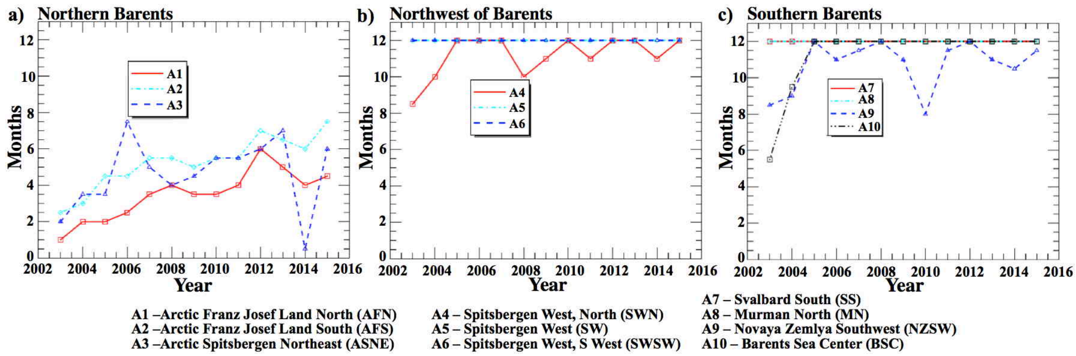

Figure 6. Ice-free months from 2003 to 2015 for focus boxes for **a)** Northern Barents (A1-A3), **b)** Northwest of Barents (A4-A6), and **c)** Southern Barents (A7-A10). Box names on panels. See **Fig. 4a** and **Supp. Table S1** for locations.

The Cryosphere Discuss., https://doi.org/10.5194/tc-2018-237
Manuscript under review for journal The Cryosphere
Discussion started: 22 November 2018

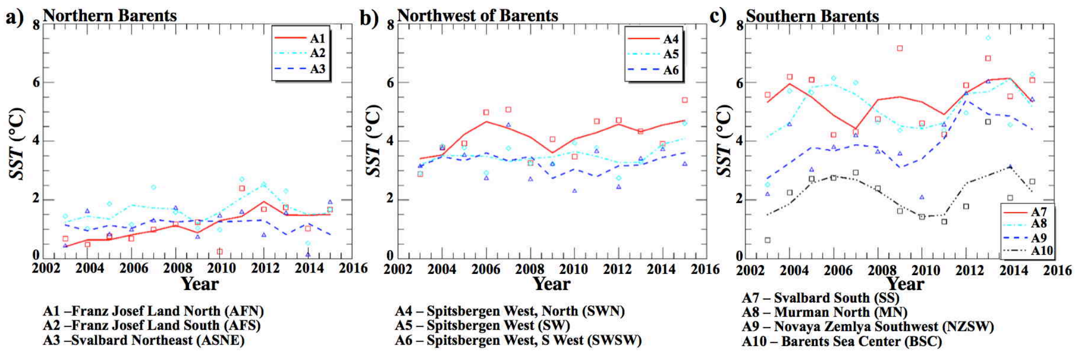

Figure 7. Sea surface temperature (*SST*) time series for 2003 to 2015 for focus box areas **a)** Northern Barents (A1-A3), **b)** Northwest of Barents (A4-A6), and **c)** Southern Barents (A7-A10). Annual values are average of all months, generally May-October, which are ice-free. Box names on panel a. Data key on figure. Lines – three year rolling averaged, symbols – no average.

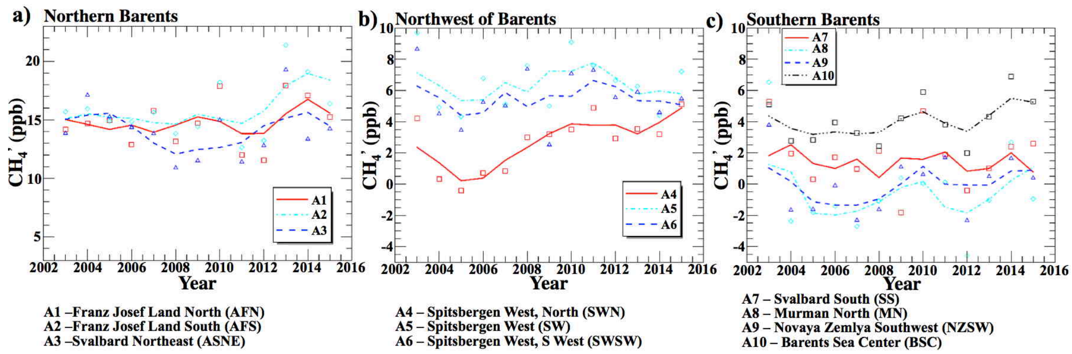

Figure 8. Focus study area methane (CH_4) for 2003 to 2015 for **a)** Northern Barents study boxes, **b)** Northwest of Barents study boxes, and **c)** Southern Barents Sea focus study boxes. Annual data and 3 year, rolling-average data shown. Anomaly is relative to entire Barents Sea. Data key on figure. Lines – three year rolling averaged, symbols – no average.

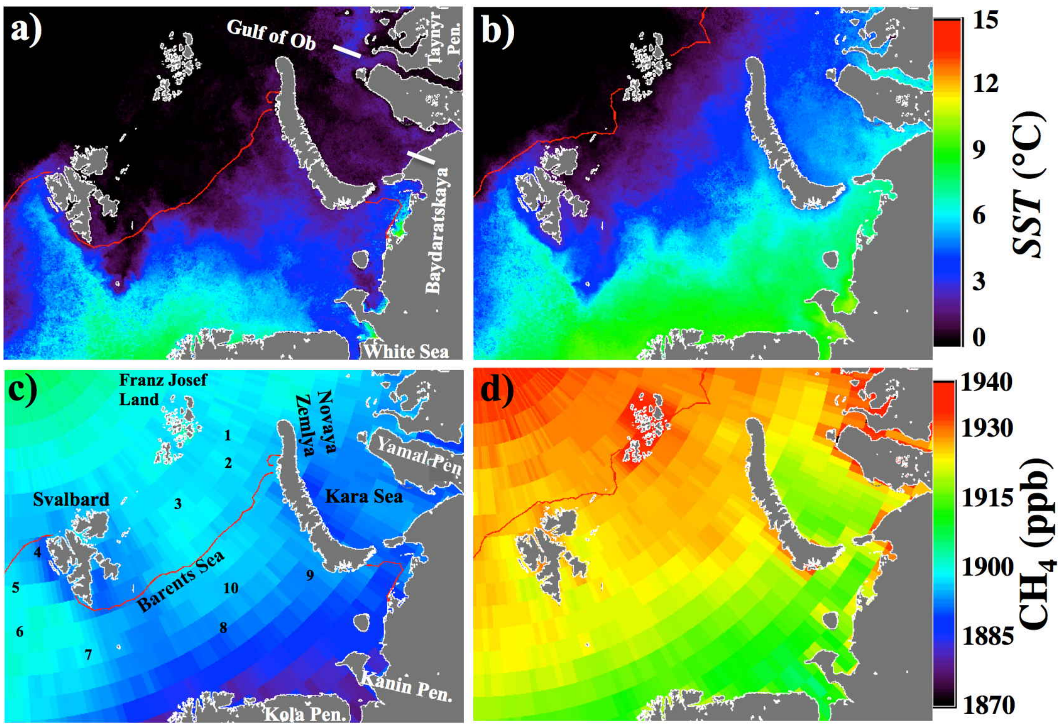

Figure 9. Mean values for 2003 to 2015 of sea surface temperature (*SST*) for **a**) June and **b**) September. Mean methane (CH_4) concentration for **c**) June and **d**) September. Median ice edge for same period is shown. Years with reduced ice extent contribute to values of *SST* north of this ice edge. Data key on figure.

The Cryosphere Discuss., https://doi.org/10.5194/tc-2018-237
Manuscript under review for journal The Cryosphere
Discussion started: 22 November 2018

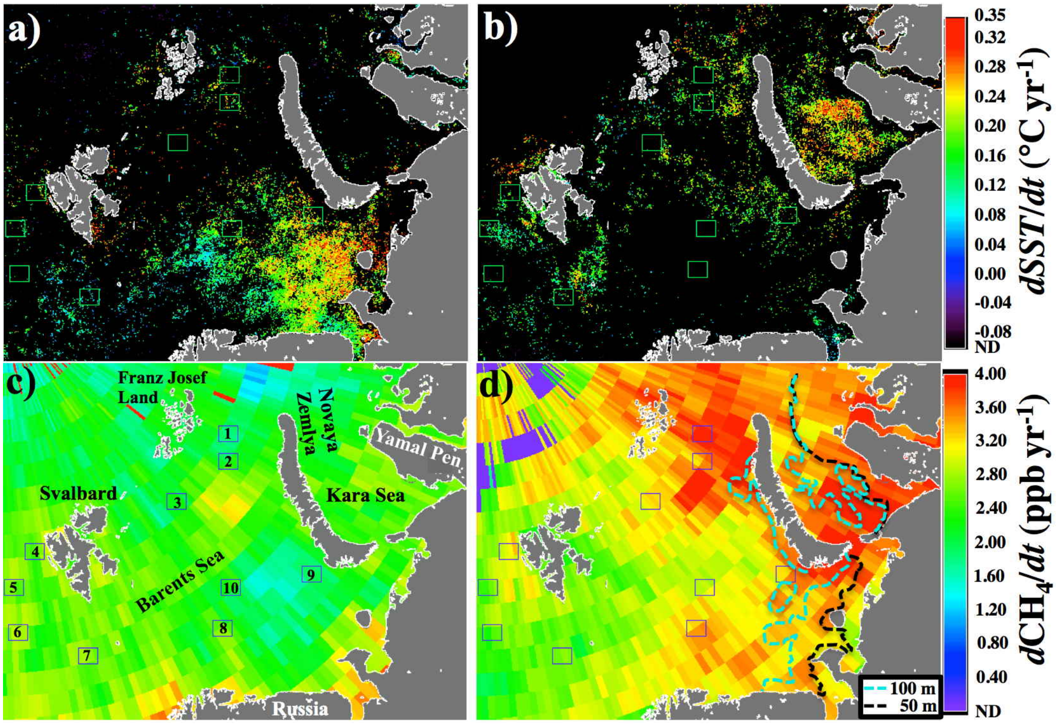

Figure 10. Linear trends for 2003 to 2015 of sea surface temperature (*dSST/dt*) for **a**) June and **b**) September. Methane concentration trend (dCH_4/dt) for **c**) June and **d**) September. ND – not detectable – failed statistical test. Blue, black dashed lines shows 100 and 50 m contour, respectively. Data key on figure.